

## RESEARCH ARTICLE

# Impacts of initial conditions and model configuration on simulations of polar lows near Svalbard using Polar WRF with 3DVAR

Jianjun Xue<sup>1,2</sup> | David H. Bromwich<sup>3</sup>  | Ziniu Xiao<sup>1</sup> | Lesheng Bai<sup>3</sup>

<sup>1</sup>State Key Laboratory of Numerical Modeling for Atmospheric Sciences and Geophysical Fluid Dynamics, The Institute of Atmospheric Physics, Chinese Academy of Sciences, Beijing, China

<sup>2</sup>University of Chinese Academy of Sciences, Beijing, China

<sup>3</sup>Polar Meteorology Group, Byrd Polar and Climate Research Center, The Ohio State University, Columbus, Ohio, USA

## Correspondence

D. H. Bromwich, Byrd Polar and Climate Research Center, 1090 Carmack Road, Columbus, OH 43210, USA.

Email: bromwich.1@osu.edu

Ziniu Xiao, State Key Laboratory of Numerical Modeling for Atmospheric Sciences and Geophysical Fluid Dynamics (LASG), The Institute of Atmospheric Physics, Chinese Academy of Sciences, 40 Huayanli, Chaoyang, Beijing, 100029, China. Email: xiaozn@lasg.iap.ac.cn

## Funding information

Chinese Academy of Sciences, Grant/Award Number: XDA20060501; National Natural Science Foundation of China, Grant/Award Number: 91937000; Office of Naval Research, Grant/Award Number: N00014-18-1-2361

## Abstract

The impacts of initial conditions and model configuration on the simulations of polar lows (PLs) near Svalbard, the global “hotspot” for PL activity, were investigated using the Polar Weather Research and Forecasting (Polar WRF or PWRF) model and WRF three-dimensional data assimilation (3DVAR). The well-documented PL case presented by Sergeev *et al.*, in 2017 from March 26, 2013 featuring *in situ* aircraft observations is revisited using PWRF and 3DVAR to identify the most suitable model configuration to simulate PLs. The simulation results using initial conditions from PWRF and 3DVAR cycling runs were compared with those of cold-start experiments using reanalysis as the initial condition. For cycling runs, the impacts of initial conditions from synoptic observations together with satellite radiances were superior to the assimilation of synoptic data alone. Several additional experiments were undertaken to further refine the PWRF configuration by considering the horizontal resolution, analysis nudging, digital filter initialization, and two boundary-layer and four microphysics schemes. Based on the chosen configuration of Polar WRF and 3DVAR from the case-study, the monthly reanalysis mode with 3 hr time window cycling data assimilation and short-term forecasts using PWRF alone were performed for March 2013 and the PLs that formed over the Nordic Seas were evaluated. Manual identification and verification of PLs were performed using thermal infrared satellite imagery and 10 m scatterometer winds. Overall, nine PLs were identified in addition to the case presented by Sergeev *et al.*, in 2017. Both the case-study and monthly simulation results show that the high-resolution initial condition is the most important factor, but a reasonable forecast model configuration can help to improve the simulation performance. Satellite radiance data are very important for producing the high-resolution initial conditions for Polar WRF to simulate PLs successfully; the best performance was obtained by assimilating both synoptic data and satellite radiances.

## KEYWORDS

comprehensive observations, data assimilation, numerical simulation, polar lows, Polar WRF

## 1 | INTRODUCTION

Polar lows (PLs) are intense mesoscale cyclones that occur over the high-latitude oceans in both hemispheres in the cold months, usually developing during marine cold air outbreaks (MCAO) (Montgomery and Farrell, 1992; Rasmussen and Turner, 2003; Kolstad, 2006; 2015; Rojo *et al.*, 2015; Stoll *et al.*, 2018). These mesoscale cyclones with strong winds and heavy precipitation constitute a threat to offshore activities such as fishing, maritime operations, and life in coastal zones of the polar regions. Yet owing to their small size (horizontal scale less than 1,000 km), short life cycle (hours to 1–2 days) and the sparse network of synoptic observations over the ocean, PLs are poorly represented in observational data, global reanalyses and numerical forecasts (Rasmussen and Turner, 2003; Zahn and von Storch, 2010; Kolstad, 2011; Iversen, 2013; Mallet *et al.*, 2013; Zappa *et al.*, 2014; Yanase *et al.*, 2015; Sergeev *et al.*, 2017; Stoll *et al.*, 2018; Radovan *et al.*, 2019).

Based on the development of reanalysis data and high-resolution numerical models during recent decades, PLs can now be investigated more comprehensively. The performance of several models was examined. For example, Zahn and von Storch (2008a) investigated the reproduction of PLs by two-year-long simulations with Climate Limited-area Model (CLM) and found “more freedom” (non-nudged) for the model was important. Wu and Petty (2010) compared five bulk microphysics schemes with Weather Research and Forecasting (WRF) simulations of PLs over the Nordic Seas and the Sea of Japan and concluded that the WRF Single-Moment 6-class (WSM6) scheme captured cloud and precipitation processes with the greatest realism. Førre *et al.* (2012) and Kolstad *et al.* (2016) discussed the roles of surface heat flux and latent-heat release in “hurricane-like” PLs over the Barents Sea using sensitivity experiments with the WRF model. Also, Adakudlu and Barstad (2011) and Kolstad and Bracegirdle (2017) explored the impacts of the ice cover and sea-surface temperature (SST) for a PL case with SST sensitivity experiments over the Barents Sea with WRF. Using Unified Model (UM) results compared to IPY–THORPEX (Kristjánsson *et al.*, 2011) data, Kristiansen *et al.* (2011) and McInnes *et al.* (2011) concluded that a horizontal grid spacing less than 4 km and the initial conditions were both important for the model performance. A detailed analysis of the structure of one shear-line PL was presented by Sergeev *et al.* (2017) using comprehensive observations and the UM. Following this, with the UM at convection-permitting grid spacing of 2.2 km, Sergeev *et al.* (2018) studied the influence of the orography of Svalbard and the sea ice cover for PL prediction over the Barents and Norwegian Seas. The effects

of grid spacing and convection representation for skilful forecasts of PLs by the limited-area model AROME-Arctic were discussed by Hallerstig *et al.* (2021) and Müller *et al.* (2017). To summarize, the following factors can be identified for successful PL numerical simulation. First, high horizontal resolution is required. Second, simulations of PL are sensitive to the initial conditions. Finally, model parametrization choices, orography, sea-ice cover and SST also play important roles.

However, to the knowledge of the authors, the results of PL simulations with Polar WRF (PWRf) and data assimilation have not been investigated in detail yet. This article seeks to investigate the effects of initial conditions and model configuration on the simulations of PL using PWRf and regional data assimilation. Therefore, a case-study of a PL near Svalbard is re-examined with a recent version of PWRf (Version 4.1.1) and three-dimensional variational data assimilation (3DVAR). Because comprehensive observations are required to validate PL simulations, the well-known PL case presented by Sergeev *et al.* (2017) that has comprehensive observations is studied again to improve the performance of PL simulations. That article, referred to as S17 below, is a key input for the present study of simulating PLs near Svalbard, and several of the figures presented here are inspired by their analyses. As the focus is on our model, we elect to include limited comparisons with their modelling results.

First, to validate and improve the performance of the PL simulations using PWRf and 3DVAR, an ensemble of sensitivity experiments is carried out for the well-documented case studied by S17 on 26 March 2013 to explore the sensitivity to horizontal resolution, initial conditions with and without data assimilation, and the impacts of the satellite radiance data assimilation in the initial conditions for PL simulation. Also, model numerical options such as analysis nudging, and digital filter initialization (DFI) along with the performance of different physical schemes (two for the planetary boundary layer (PBL) and four for microphysics) are evaluated by comparison with satellite and *in situ* observations.

Next, to examine the performance of simulated PLs during a long period, monthly simulations using PWRf only with the initial conditions directly from ERA-Interim, and a monthly cycling data assimilation using PWRf and 3DVAR with synoptic observations alone and combined with satellite radiances, are performed for March 2013. The refined configurations of PWRf and 3DVAR from the case-study are used for the monthly runs. The PLs that formed over the Nordic Seas are evaluated by manual identification and verification using Advanced Very-High Resolution Radiometer (AVHRR) 4 km thermal infrared satellite imagery and 12.5 km resolution 10 m wind fields from the Advanced Scatterometer (ASCAT).

The structure of the article is as follows. Section 2 describes the model, experiment strategy and data used in this study. Section 3 discusses the results of the sensitivity experiments for the S17 case-study. The manual identification of PLs and the performance of each month-long simulation approach are given in Section 4. Finally, a discussion and summary are provided in Section 5.

## 2 | MODEL, EXPERIMENTAL DESIGN AND DATA

### 2.1 | Polar WRF

The model used in this study is the polar-optimized version of the WRF model that is known as Polar WRF (PWRf) (e.g., Hines *et al.*, 2011). It focuses on the environmental characteristics of the polar regions such as optimal treatment of heat transfer for ice sheets and revised surface energy balance calculation in the Noah Land Surface model (e.g., Ek *et al.*, 2003), comprehensive description of sea ice, and improved cloud microphysics for polar conditions with many of these improvements now being part of the standard release of WRF (e.g., Hines and Bromwich, 2008; 2017; Bromwich *et al.*, 2009; Hines *et al.*, 2011; 2015). Moreover, PWRf and WRF-3DVAR cycling data assimilations have been used to produce the Arctic System Reanalysis (ASRv1 and ASRv2: Bromwich *et al.*, 2016; 2018); ASR has been applied to investigate PLs and found to represent PLs much better than other reanalyses (Smirnova and Golubkin, 2017; Stoll *et al.*, 2018).

Hence, based on a wide range of studies of WRF/PWRf over the polar regions (Hines and Bromwich, 2008; Bromwich *et al.*, 2009; 2018; Wu and Petty, 2010; Hines *et al.*, 2011), the Kain–Fritsch scheme (Kain, 2004) is used for cumulus parametrization when model horizontal resolution is greater than 5 km, and the global model version of the Rapid Radiative Transfer Model (RRTMG) describing long-wave and short-wave radiation (Iacono *et al.*, 2008) is selected. The Noah Land Surface model with the polar updates optimized from Hines and Bromwich (2008) is used in this study. Two PBL schemes are considered: the new version Mellor–Yamada–Nakanishi–Niino (MYNN) 2.5-level scheme that improves downward short-wave radiation at the surface (Olson *et al.*, 2019) in WRF version 4.1.1, and the Mellor–Yamada–Janjić (MYJ) turbulent kinetic energy scheme (Janjić, 1994) which widely was tested by the Polar Meteorology Group (Hines *et al.*, 2011; Bromwich *et al.*, 2013) and demonstrated good skill for wind forecasts over Svalbard (Kim *et al.*, 2019). The following microphysics options are investigated based on several (PL) modelling studies (Wu and Petty, 2010;

Wu *et al.*, 2011; Førre *et al.*, 2012; Kolstad *et al.*, 2016; Hines and Bromwich, 2017; Hines *et al.*, 2019): the Morrison-2-moment, a scheme that has been extensively tested in the polar regions and shown good performance; the Morrison–Milbrandt P3 scheme (P3) (Morrison and Milbrandt, 2014), that produced greater liquid water content than Morrison-2-moment in central West Antarctica (Hines *et al.*, 2019); the aerosol-aware Thompson microphysics (Thompson and Eidhammer, 2014); and WRF double-moment six-class scheme (WDM6: Lim and Hong, 2009), an advance on WSM6 studied by Wu and Petty (2010). The parametrizations are summarized in Table 1.

Nudging, a method of pushing simulations toward analysis or observation, has been widely used for numerical simulation of PLs (Zahn and von Storch, 2008a; 2008b; Kolstad *et al.*, 2016). Unsuitable nudging may damage the sensitivity to latent heating at upper levels and prohibit the development of extreme events, both of which would suppress the growth of PLs (Cha *et al.*, 2011; Glisan *et al.*, 2012; Otte *et al.*, 2012; Kolstad *et al.*, 2016). For spectral nudging, the small scales are more sensitive to wave numbers determined by the size of the modelling domain and the scale of driving forces (Liu *et al.*, 2012). It is also not recommended when dynamic aspects need to be addressed, such as during the genesis of a storm (von Storch *et al.*, 2000). Grid nudging is a “simple” but effective option that has been stressed as providing good precipitation and moisture adjustment (Bowden *et al.*, 2012; Wootten *et al.*, 2016), and is used here to prevent the simulations from drifting away from large-scale driving fields (ERA-Interim).

### 2.2 | Data assimilation

#### 2.2.1 | WRF-3DVAR

PLs typically form when cold dry air from Arctic sea ice moves over the warmer open ocean. Usually there is a shortage of *in situ* observations in this region. Therefore, it is still challenging to analyse the detailed structure of PLs, as well as to provide the high-resolution initial conditions to simulate and forecast these small-scale and explosive weather phenomena accurately (Yanase and Niino, 2007; Zahn and von Storch, 2008b; Kristiansen *et al.*, 2011; Sergeev *et al.*, 2017). Data assimilation (DA) is the technique that combines observations and short-term model forecasts to provide an estimate of atmospheric conditions valid at a prescribed analysis time. Currently, WRF Data Assimilation System (WRFDA) has been extended to include a broad range of DA techniques, such as 3DVAR, 4DVAR and EnVar (Barker *et al.*, 2004; 2012; Huang *et al.*, 2009). In this study, WRFDA-3DVAR is selected

**TABLE 1** Summary of the model settings and experimental method

<b>PWRF V4.1.1</b>	
Horizontal resolution	3/6/9 km
Vertical level	71 levels, the model top level at 3 hPa
Coordinate	Hybrid Vertical Coordinate, eta = 0.3
Land surface options	Noah
Short/long-wave	Both RRTMG
Cumulus	Kain–Fritsch when model horizontal resolution is greater than 5 km
Microphysics	Morrison-2-mom/P3/aerosol-aware Thompson/WDM6
PBL scheme	MYNN2 /MYJ
Surface layer	MYNN when PBL Scheme is MYNN2. Monin–Obukhov when PBL Scheme is MYJ
Nudging	Grid nudging $t, ph, u, v$ , above 550 hPa, coefficient: 0.0001
Lateral/bottom boundary data	Atmospheric and soil information: ERA-Interim. SST and sea ice: OSTIA, $0.05^\circ \times 0.05^\circ$
<b>WRFDA V4.1</b>	
Method	3DVAR, assimilation of observations within $\pm 1.5$ hr.
Background error	Computed for the whole month based on 12 and 24 hr PWRF forecasts
Data	Typical conventional observations GPS radio occultations Radiances: AMSU-A, MHS sensors are selected.
<b>Experimental method</b>	
Cold start	PWRF, spin-up 24/12 hr
Cycling runs	WRFDA and PWRF, regional cycling assimilation every 3 hr

because it is simpler and much less computationally demanding than WRFDA-4DVAR and EnVar, as well as more mature and reliably examined in the polar regions such as in the ASR and the Antarctic Mesoscale Prediction System (Powers *et al.*, 2012; Bromwich *et al.*, 2016; 2018).

### 2.2.2 | Observations for data assimilation

Conventional *in situ* data and satellite-derived winds from the Global Telecommunications System (GTS) are used. Surface data include surface pressure, temperature and specific humidity at 2 m, and  $u$ -wind and  $v$ -wind components at 10 m from synoptic weather stations (SYNOP) and airport stations (METAR) over land, and also from buoys (BUOY) and ships (SHIPS) over the ocean. Upper air data consist of  $u$ -wind and  $v$ -wind from profilers (PROFILER);  $u$ -wind,  $v$ -wind, temperature and specific humidity from radiosondes (SOUND);  $u$ -wind,  $v$ -wind and temperature from aircraft (AIREP); and  $u$ -wind and  $v$ -wind components from satellite cloud-track wind products retrieved from polar-orbiting and geostationary satellites (SATOBS). A snapshot of the distribution of these

types of observations at 1200 UTC on March 26, 2016 is displayed in Figure 1b.

Advanced Microwave Sounding Unit A (AMSU-A) radiances from NOAA-15, -18, -19 and MetOp-2 satellites are used for the data assimilation, and the Microwave Humidity Sounder (MHS; Barker *et al.*, 2012) is also used. AMSU-A is a cross-track, line-scanned microwave sensor with 15 channels, each with a 2,343 km swath width. It measures 30 pixels in each swath with an approximate 48 km diameter footprint at nadir. In this study, window channels 1–4 and 15 were not assimilated due to their large sensitivities to uncertain surface parameters (e.g., surface emissivity and skin temperature). High-peaking channels 10–14 were also excluded considering the 3 hPa model top. Therefore, only temperature-sensitive channels 5–9 were assimilated. A snapshot of AMSU-A radiances from four satellites within a 3 hr time window centred at 1200 UTC March 26, 2013 is displayed in Figure 1a. All these observations are provided by the National Centers for Environmental Prediction (NCEP) in the binary universal form for the representation of meteorological data (BUFR) format and are assimilated by WRF-3DVAR within a  $\pm 1.5$  hr time window (Figure 1) to provide the high-resolution initial conditions for the simulations of PLs by Polar WRF.



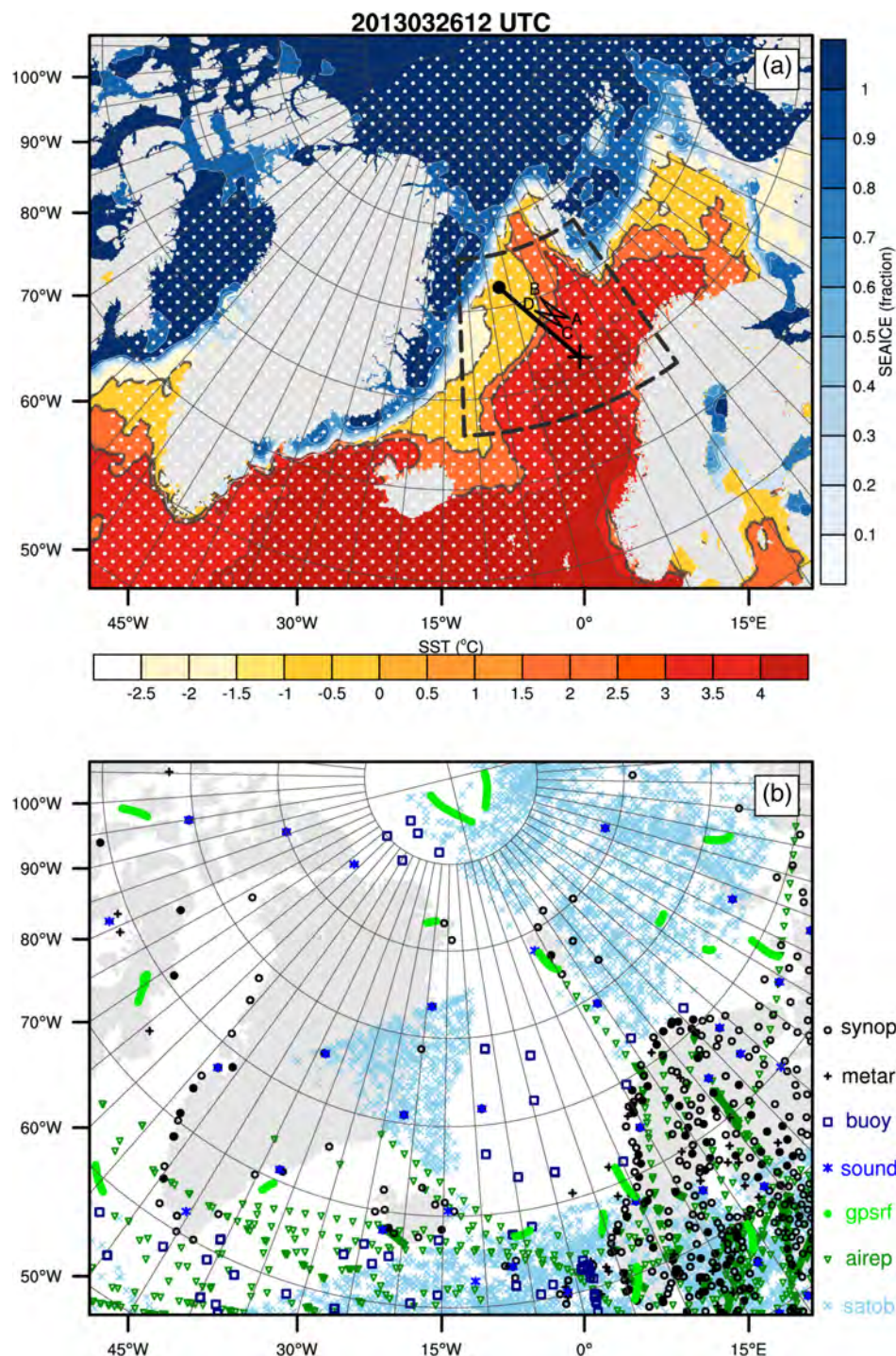


**FIGURE 1** (a) Modelling domain with sea ice and SST derived from OSTIA (0.05°×0.05°) along with the coverage of AMSU-A data (white dots, NOAA-16). The black dashed box indicates the focus region for the S17 case-study with the flight tracks (blue lines, A–B–C–D–A) and CloudSat swath (black line) used in this investigation. (b) Non-radiance data available for assimilation within ±1.5 hr time window [Colour figure can be viewed at wileyonlinelibrary.com]

## 2.3 | Experimental design

### 2.3.1 | Domain, initial conditions, lower and lateral boundary conditions

The Nordic Seas (i.e. the Greenland, Norwegian and Barents Seas) are one of the main development regions for PLs during the extended boreal winter (November–April) (e.g., Adakudlu and Barstad, 2011; Kolstad, 2011; 2015; Førre *et al.*, 2012; Smirnova *et al.*, 2015; Sergeev *et al.*, 2018;

Stoll *et al.*, 2018; Landgren *et al.*, 2019). The sparse coverage of conventional observations at high latitudes always complicates PL study. Fortunately, multiple PL events around the Svalbard archipelago were observed during the Aerosol–Cloud Coupling And Climate Interactions in the Arctic (ACCACIA) field campaign in March–April 2013 (Sergeev *et al.*, 2017), and a representative case was investigated by S17. It is known that the appropriate experimental domain is important to the PL simulations (Kristiansen *et al.*, 2011). Hence, the single model domain used here

**TABLE 2** Summary of the characteristics of each model experiment

Abbreviation	Microphysics	PBL scheme	Nudging strength	Start time (UTC)	Comments (compared to control)
Cold start					
CS-24	Morrison2-mom <sup>a</sup> 50	MYJ	0.0001	25.00	Control
CS-12	Morrison2-mom <sup>a</sup> 50	MYJ	0.0001	25.12	Initialization time
Cycling runs					
CR	Morrison2-mom <sup>a</sup> 50	MYJ	0.0001	25.00	Control, radiances, moderate nudging
CR-NS	Morrison2-mom <sup>a</sup> 50	MYJ	0.0003	25.00	Strong nudging
CR-NW	Morrison2-mom <sup>a</sup> 50	MYJ	0.00003	25.00	Weak nudging
CR-6 km	Morrison2-mom <sup>a</sup> 50	MYJ	0.0001	25.00	6 km horizontal resolution
CR-NR	Morrison2-mom <sup>a</sup> 50	MYJ	0.0001	25.00	No radiances
CR-DFI	Morrison2-mom <sup>a</sup> 50	MYJ	0.0001	25.00	Using DFI
CR-MYNN	Morrison2-mom <sup>a</sup> 50	MYNN	0.0001	25.00	PBL MYNN
CR-M10	Morrison2-mom <sup>a</sup> 10	MYJ	0.0001	25.00	Liquid water droplet concentration 10 cm <sup>-3</sup>
CR-M100	Morrison2-mom <sup>a</sup> 100	MYJ	0.0001	25.00	Liquid water droplet concentration 100 cm <sup>-3</sup>
CR-P3	P3	MYJ	0.0001	25.00	Microphysics P3
CR-T	Thompson aerosol-aware	MYJ	0.0001	25.00	Microphysics Thompson aerosol-aware
CR-W	WDM6	MYJ	0.0001	25.00	Microphysics WDM6

<sup>a</sup>Liquid water droplet concentration specified in Morrison 2-moment microphysics scheme.

covers the Nordic Seas, surrounding Greenland, Iceland, and part of continental Europe where the influences of orography, sea ice, and strong and frequent MCAOs can be well sampled (Figure 1). The model is set up with horizontal resolutions of 3/6/9 km. The model vertical resolution is 71 levels with a model top at 3 hPa, the first model level at about 4 m above the surface and 26 levels below 850 hPa (Table 1).

PLs are sensitive to sea ice and sea-surface temperature (SST), via their influence on low-level baroclinicity and surface heat fluxes as revealed by previous studies (e.g., Adakudlu and Barstad, 2011; Kolstad and Bracegirdle, 2017; Sergeev *et al.*, 2018; Stoll *et al.*, 2020). Therefore, high-quality sea-ice and SST fields were derived from the Operational Sea Surface Temperature and Sea Ice Analysis (OSTIA) at 0.05° × 0.05° resolution daily dataset downscaled to the model resolution are used for both the cycling data assimilation and PWRP simulations and are updated every 3 hr. For atmospheric and soil information, data interpolated from the ERA-Interim (Dee

*et al.*, 2011) atmospheric reanalysis fields (60 model levels) which demonstrated better performance in polar regions and PL simulation studies (Bromwich *et al.*, 2013; 2018; Kolstad *et al.*, 2016; Kolstad and Bracegirdle, 2017) are used to provide initial conditions and lateral boundary conditions for the data assimilation and PWRP forecast simulation. The ERA-Interim reanalysis land data are used to provide the lower boundary conditions for 3DVAR and Polar WRF.

### 2.3.2 | Experimental strategy

The characteristics of each sensitivity experiment for the case-study are listed in Table 2. Two methods are utilized: one is only with PWRP (referred to as Cold Start or CS) and the other is analysis-forecast cycling, with PWRP and WRFDA-3DVAR cycling together (referred to as Cycling Runs or CR). For CS runs, the model was initialized at 0000 UTC/1200 UTC from ERA-Interim



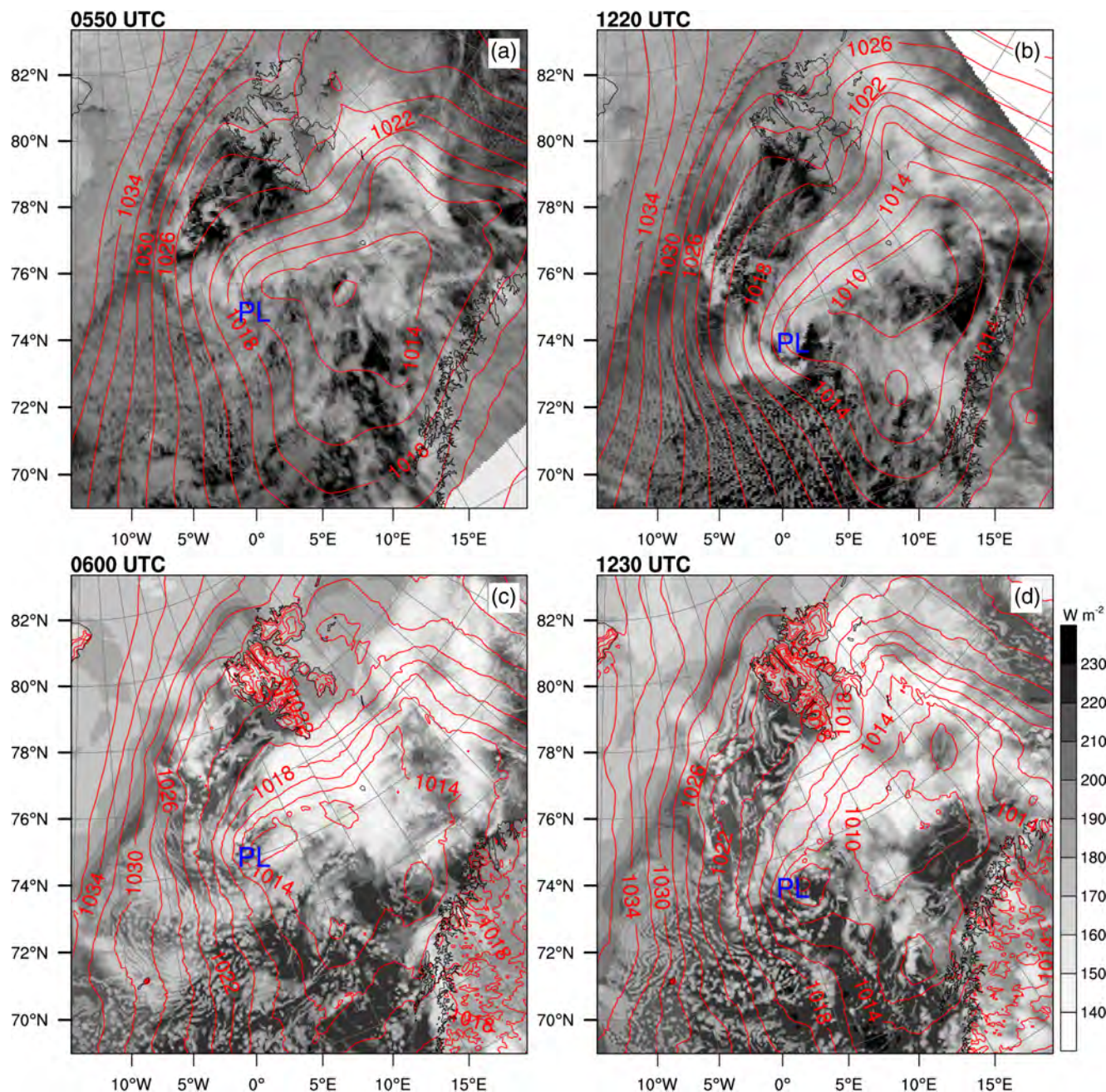


**FIGURE 2** (a,b) Channel 4 imagery from AVHRR NOAA-19 (0550 and 1220 UTC 26 March 2013) overlaid by ERA-Interim sea-level pressure (SLP, red lines, hPa) at 0600 and 1200 UTC. (c,d) OLR of CR experiment at 0600 and 1230 UTC 26 March overlaid by sea-level pressure (SLP, red lines, hPa). The blue capital letter PL indicates the approximate position of the polar low [Colour figure can be viewed at [wileyonlinelibrary.com](http://wileyonlinelibrary.com)]

with the first 24 hr/12 hr of output discarded as model spin-up and the following 24 hr PWRP forecast analysed. The CR was made at 3 hr intervals (0000, 0300 UTC, etc.) from the analysis–forecast cycling with the PWRP and WRFDA-3DVAR, and the 3 hr forecasts generated by PWRP are used for comparison. To identify the optimal model parameter settings, the following aspects were examined with sensitivity runs. To evaluate different initialization times which was emphasized as critical for

this small-scale PL by S17, two Cold Start experiments (CS-24/12) were performed. In the group of CR runs, the impact of assimilating the synoptic observation data together with satellite radiances and the synoptic data only was examined by CR and CR-NR, respectively. Control runs using 6 km grid spacing (CR-6 km), strong/weak nudging (CR-NS/CR-NW), and DFI option (CR-DFI) also were undertaken to verify the role of spatial resolution, the strength of nudging and the impact of DFI,



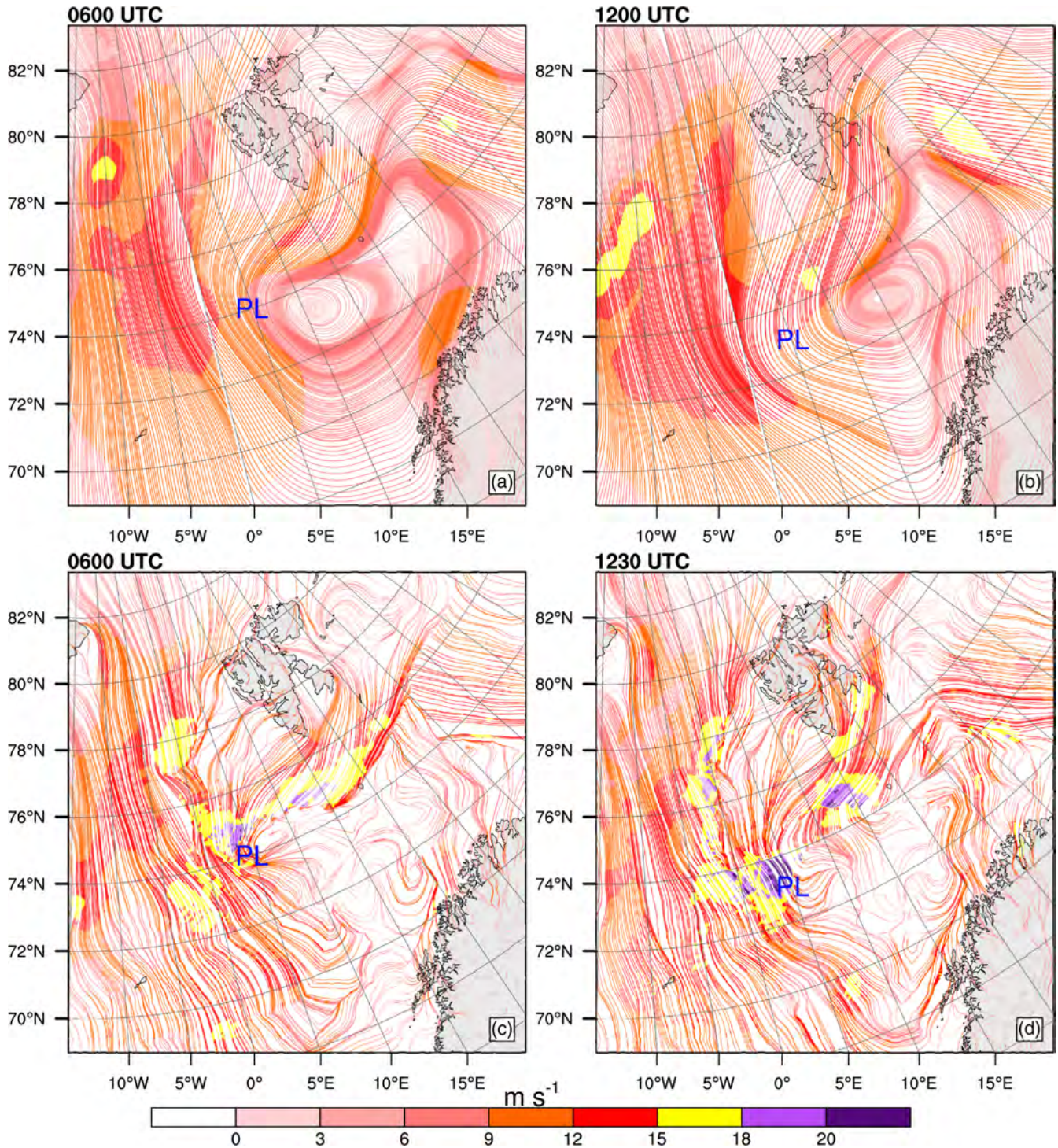


**FIGURE 3** (a,b) Ten-metre winds from ERA-Interim at 0600 and 1200 UTC 26 March, (c,d) 10 m wind field of CR experiment at 0600 and 1230 UTC. The blue PL label locates the approximate position of the polar low [Colour figure can be viewed at [wileyonlinelibrary.com](http://wileyonlinelibrary.com)]

respectively. For the PBL, the MYNN 2.5-level has been used in polar region studies including for PLs (Bromwich *et al.*, 2016; Kolstad *et al.*, 2016), and is especially recommended when simulating terrain effects over Svalbard (Claremar *et al.*, 2012). However, if the model domain contains flat regions (such as the open ocean), MYJ

performs well (Kilpeläinen *et al.*, 2011; Kolstad, 2015; Kim *et al.*, 2019). Therefore, simulations with the MYJ (CR) and MYNN (CR-MYNN) schemes were undertaken to determine which is better. For microphysics, following Hines and Bromwich (2017) and Hines *et al.* (2019), the two-moment Morrison scheme with liquid water



**TABLE 3** The minimum SLP, the surface maximum wind speed at 10 m, the maximum relative vorticity at 950 hPa, the maximum latent-heat flux, the maximum sensible-heat flux and the maximum SST–T500 calculated from the PL region (box areas in Figures 4 and 5, 72–74°N, 2–10°E) at 1300 UTC 26 March 2013

Experiments	Min SLP (hPa)	Max WS (m·s <sup>-1</sup> )	Max RV 950 hPa (10 <sup>-4</sup> s <sup>-1</sup> )	Max LHF (W·m <sup>-2</sup> )	Max SHF (W·m <sup>-2</sup> )	Min SST-T500 (°C)
CR	1,008	23	48	457	590	44
CR-DFI	1,008	22	34	426	541	44
CR-NR	1,008	21	35	357	390	46
CR-6 km	1,009	18	12	372	565	45
CS-12	1,009	24	40	368	453	45

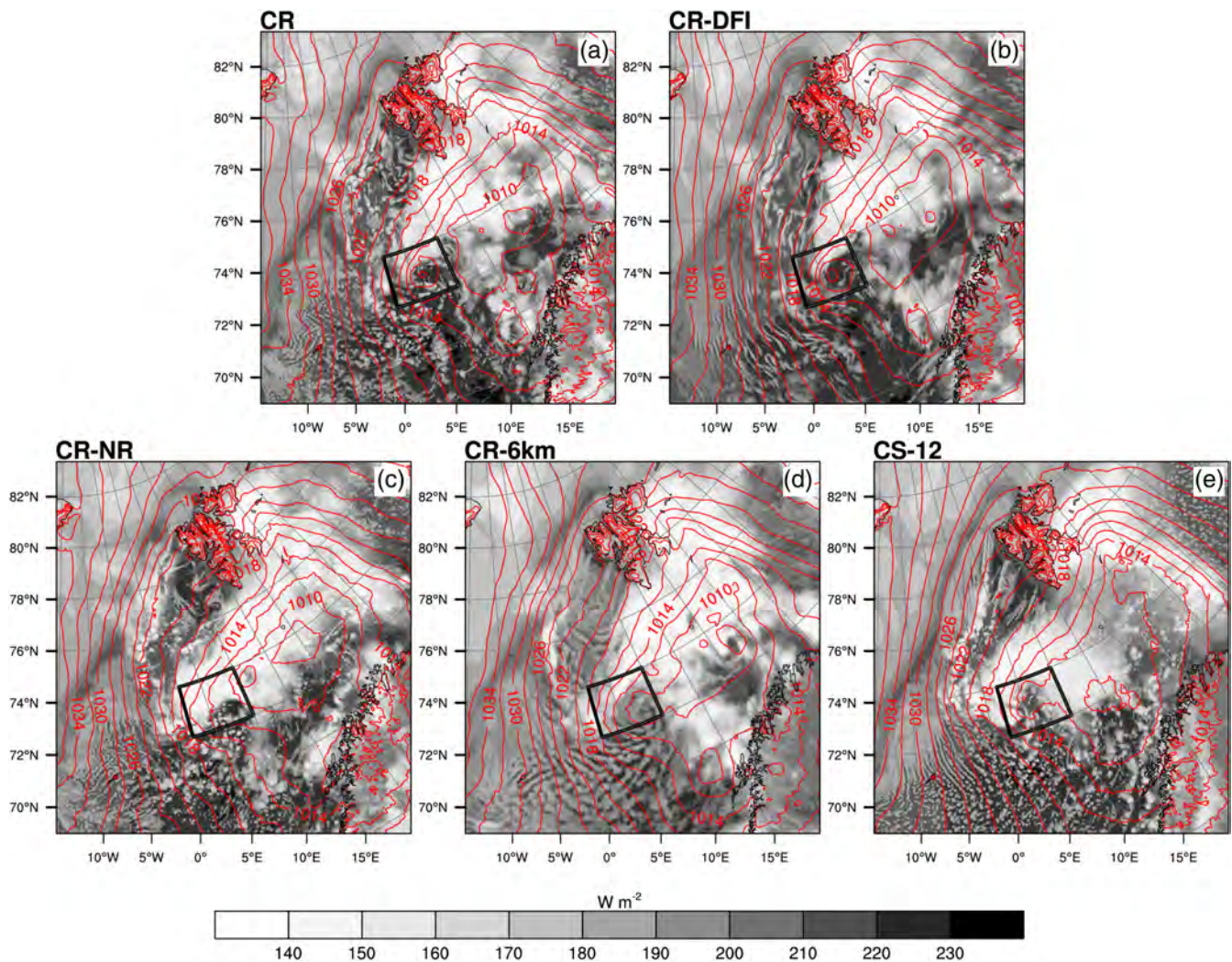


**FIGURE 4** OLR (W·m<sup>-2</sup>) overlaid by SLP (red contours, hPa) for five model sensitivity experiments at 1300 UTC 26 March: (a) CR, (b) CR-DFI, (c) CR-NR, (d) CR-6 km, and (e) CS-12. The characteristics of each experiment are given in Table 2. The blue box indicates the approximate position of the polar low [Colour figure can be viewed at [wileyonlinelibrary.com](http://wileyonlinelibrary.com)]

droplet concentrations reduced from the standard value of 250 to 100 cm<sup>-3</sup>, 50 and 10 cm<sup>-3</sup> were evaluated (CR-M100, CR and CR-M10). The P3 scheme that has been available since the fourth version of WRF (Morrison

and Milbrandt, 2014; Milbrandt and Morrison, 2015) was also examined (CR-P3). Considering the Thompson and WSM6 schemes have been extensively tested and are known for their ability to simulate PLs (e.g., Lim and



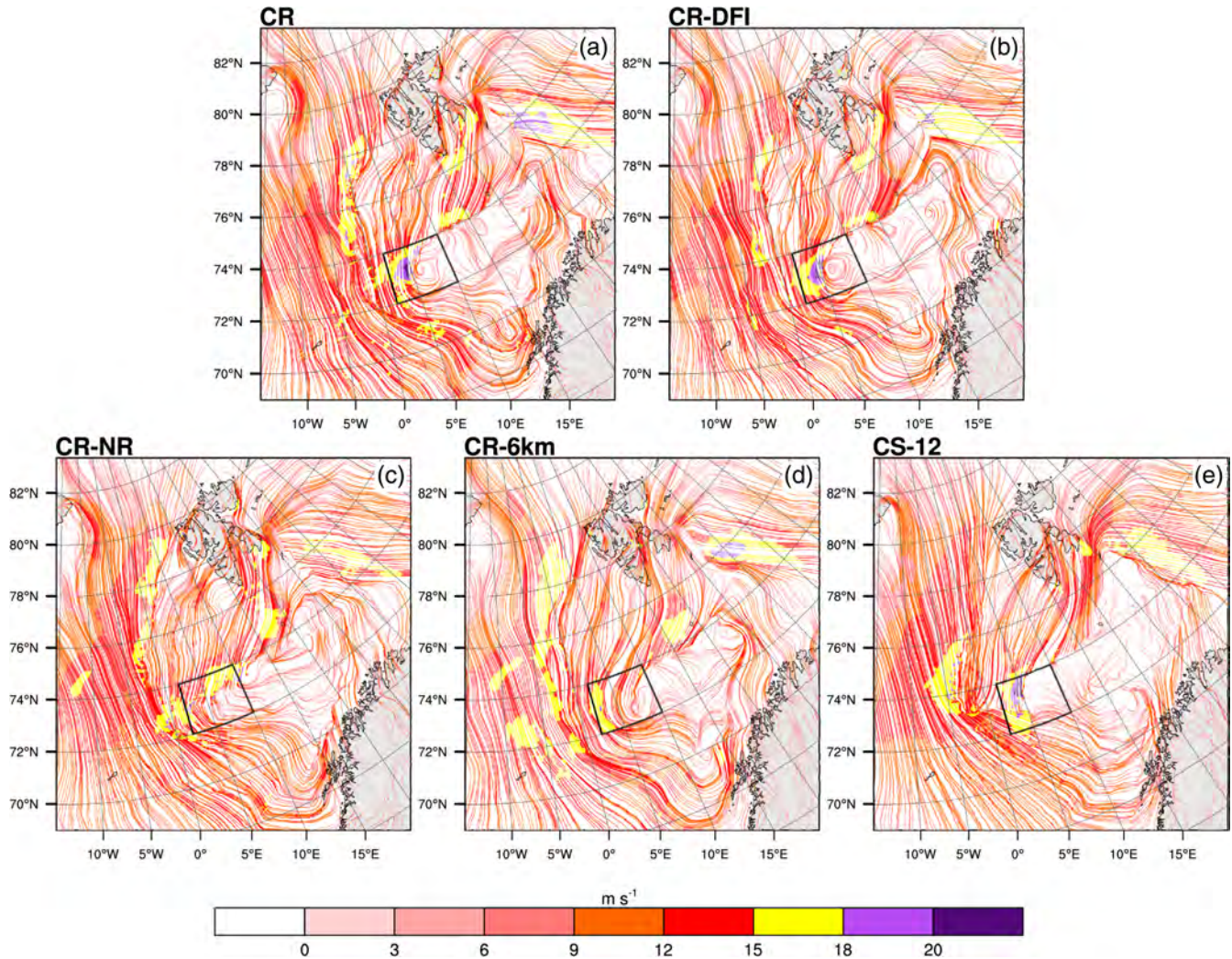


**FIGURE 5** Wind speed ( $\text{m s}^{-1}$ ) at 10 m of five model sensitivity experiments at 1300 UTC 26 March: (a) CR, (b) CR-DFI, (c) CR-NR, (d) CR-6 km, and (e) CS-12. The characteristics of each experiment are given in Table 2. The black box indicates the approximate position of the polar low [Colour figure can be viewed at [wileyonlinelibrary.com](http://wileyonlinelibrary.com)]

Hong, 2009; Wu and Petty, 2010; Thompson and Eidhammer, 2014; Hines *et al.*, 2019), the aerosol-aware Thompson and WDM6 that are advanced over the earlier versions are also performed (CR-T, CR-W). Unlike Cold Start runs, all Cycling Run simulations were initialized at 0000 UTC 25 March to allow the assimilated observations to have greater impact on the short-term forecasts. The model output frequency was 30 min from 0900 to 1500 UTC on 26 March.

To evaluate the capabilities of long-term simulations, three additional sensitivity experiments using PWRP alone, PWRP with 3DVAR assimilating solely synoptic observations and both synoptic observations and satellite radiances were investigated with month-long simulations of PLs during March 2013. The details are discussed in Section 4.

## 2.4 | Validation data

### 2.4.1 | Satellite data

Satellite data are especially useful for the analysis of PLs. Due to the scarcity of *in situ* observations, satellite data provide direct imagery and estimate meteorological variables from different remote-sensing instruments such as cloud composition and surface winds. Here, three types of satellite data contributed to this study.

The PL imagery is obtained from the AVHRR instrument. It is subsampled to produce reduced-resolution Global Area Coverage (GAC) data. The spatial resolution is actually  $4.4$  (across-track)  $\times$   $1.1$  (along-track) km generated by averaging raw sensor counts with  $3 \times 5$  arrays spread over three scan lines (Heidinger *et al.*, 2014), here



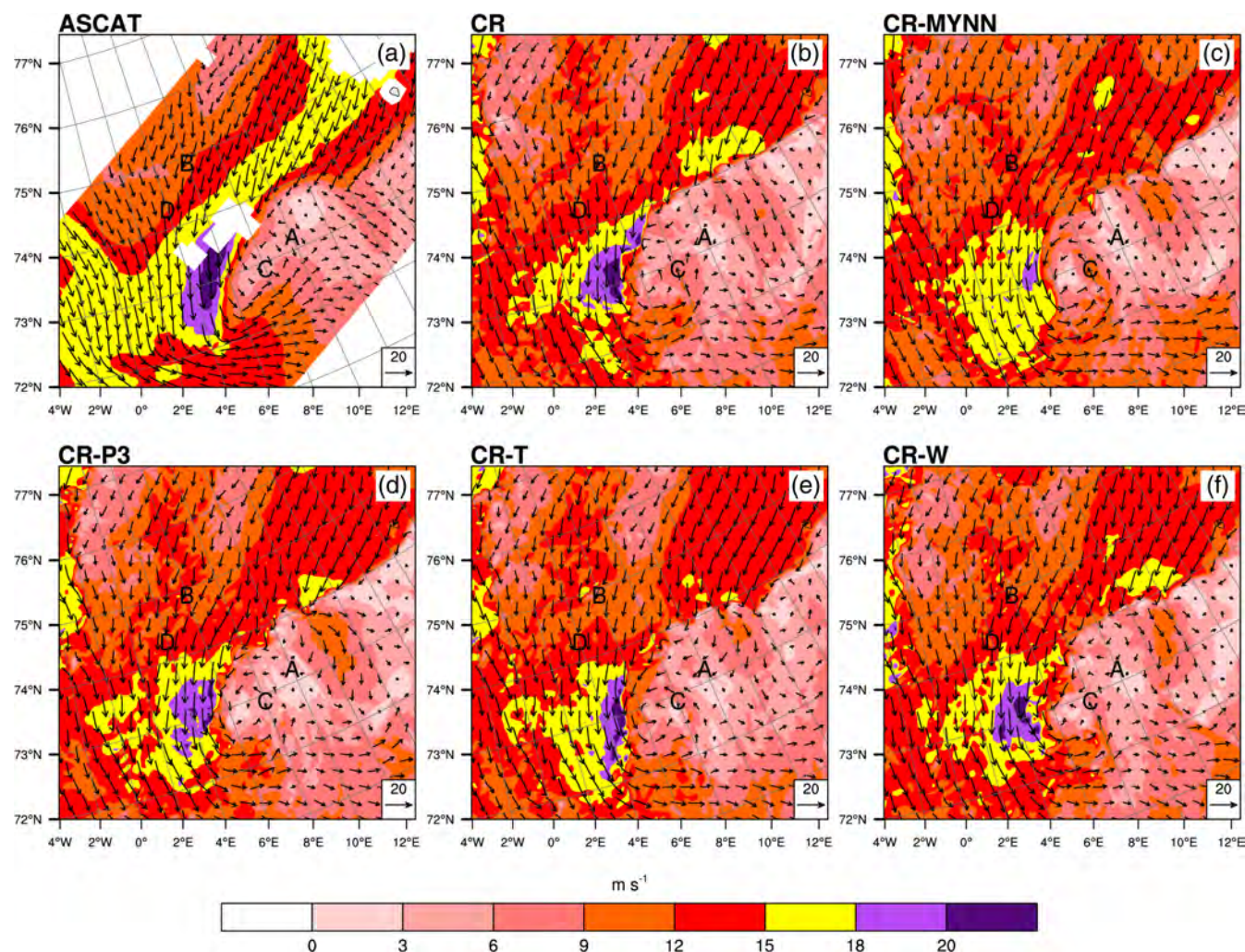


**FIGURE 6** Wind speed ( $\text{m s}^{-1}$ ) and direction at 10 m from ASCAT and model output at 1300 UTC 26 March: (a) estimated by ASCAT, (b) CR, (c) CR-MYNN, (d) CR-P3, (e) CR-T, and (f) CR-W. The characteristics of the five experiments are given in Table 2. The black capital letters (A B C D) indicate the approximate operating area of the aircraft (same as Figure 1) [Colour figure can be viewed at [wileyonlinelibrary.com](http://wileyonlinelibrary.com)]

summarized as 4 km resolution. Generally, the satellite passes over this region several times each day and some images are available for PL identification. For instance, images covering the Norwegian Sea and fully capturing the PL cloud features around 0550 and 1220 UTC on 26 March 2013 are shown in Figure 2a,b.

Near-gale force surface winds are a notable feature of PLs. From the scatterometer instruments on MetOp-A, the 12.5 km product of the near-surface ocean wind vector is derived and has been widely applied to PL studies (e.g., Noer *et al.*, 2011; Furevik *et al.*, 2015). Over the area of interest, ASCAT provides 10 m surface winds in  $\sim 518$ -km-wide swaths each day that can be used for PL validation.

CloudSat is a satellite experiment designed to measure the vertical structure of clouds globally. The 94 GHz spaceborne cloud-profiling radar provides cloud

profile information, such as radar reflectivity, liquid water content (LWC) and ice water content (IWC) profiles with 240 m vertical resolution and  $1.4 \times 1.7$  km footprint size. Although CloudSat repeats the same ground track every 16 days and completes 14 Equator overpasses on a daily basis, for the case of S17, an orbit passed exactly over this area only once (around 1130 UTC, see Figure 1a, the cross is the start point and dot is end point of the data used) (Stephens *et al.*, 2002; Tourville *et al.*, 2014; Sergeev *et al.*, 2017).

## 2.4.2 | Aircraft observations

Direct observations from the Facility for Airborne Atmospheric Measurements (FAAM) BAe-146 aircraft during flight B763 on 26 March 2013 are used for the S17



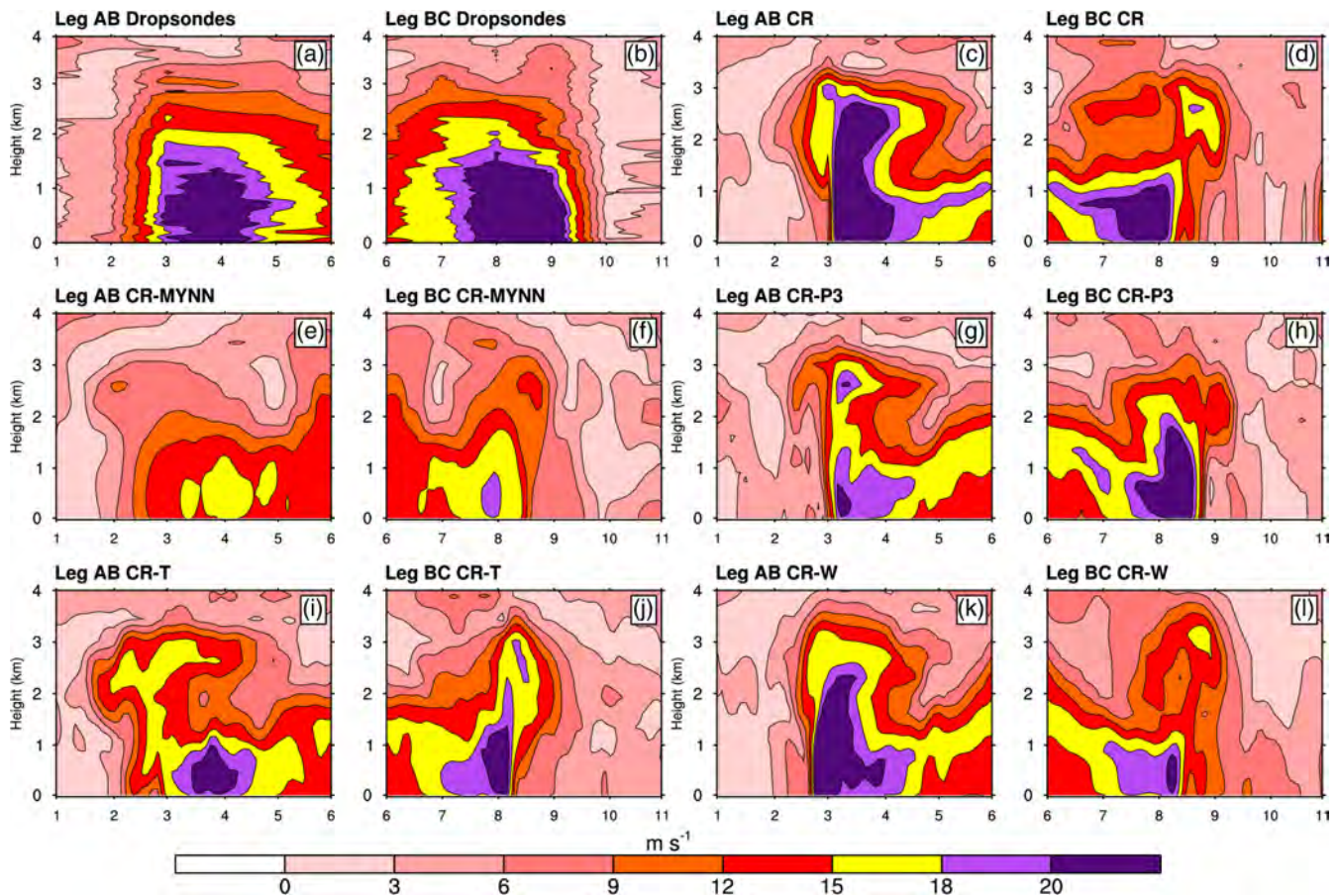


**FIGURE 7** Vertical cross-sections of wind speed ( $\text{m}\cdot\text{s}^{-1}$ ) along with Legs AB and BC from dropsondes and model output at 1130 UTC 26 March (similar to S17). The positions of A, B and C are shown in Figure 6. (a,b) Interpolated dropsonde soundings, Leg AB used dropsondes 1–6, Leg BC used dropsondes 6–11. (c,d) CR, (e,f) CR-MYNN, (g,h) CR-P3, (i,j) CR-T, and (k,l) CR-W. Numbers on the x-axis identify the dropsondes [Colour figure can be viewed at [wileyonlinelibrary.com](http://wileyonlinelibrary.com)]

case-study. The flight took off at 0958 UTC and landed 5 hr later to map out the PL that developed near Svalbard approximately within  $73\text{--}75^\circ\text{N}$ ,  $7\text{--}14^\circ\text{E}$ . The flight track followed a “butterfly” pattern (A–B–C–D–A, see Figure 1) with measurements lasting from 1100 to 1400 UTC. Eleven Vaisala RD93 dropsondes were released along legs AB and BC from 1121 to 1221 UTC about every 5 min at an altitude of  $\sim 6,000$  m above sea level (ASL). Detailed information is provided by the flight log available from the FAAM data website (<https://catalogue.ceda.ac.uk/uuid/177bb10225aa45fa9edcb3169f5f3c27>).

### 2.4.3 | Reanalysis data

Although reanalysis datasets generally do not represent PL accurately, especially for the smallest systems with diameters less than 200 km (Zappa *et al.*, 2014; Yanase *et al.*, 2015; Smirnova and Golubkin, 2017; Stoll *et al.*, 2018), they do capture the broadscale state of the atmosphere, which helps to understand the background

conditions of PL. Here, the variables of sea-level pressure (SLP) and  $U$  and  $V$  wind components derived from ERA-Interim (Dee *et al.*, 2011) are used for investigation of the S17 case-study.

## 3 | RESULTS

### 3.1 | Case-study overview

The well-documented PL investigated by S17 is re-examined here. Figure 2a,b show the AVHRR imagery from NOAA-19 at 0550 and 1220 UTC on March 26, 2013 overlaid with the SLP from ERA-Interim at nearly the same time. It is clear that the satellite images well depicted the cloud features and the comma cloud band structure showing the temporal development of the PL. Although the SLP and wind streamlines (Figure 3a,b) of ERA-Interim failed to resolve the PL, the circulation reveals an intense southward cold Arctic air outbreak. The resulting strong baroclinic zone favours the development



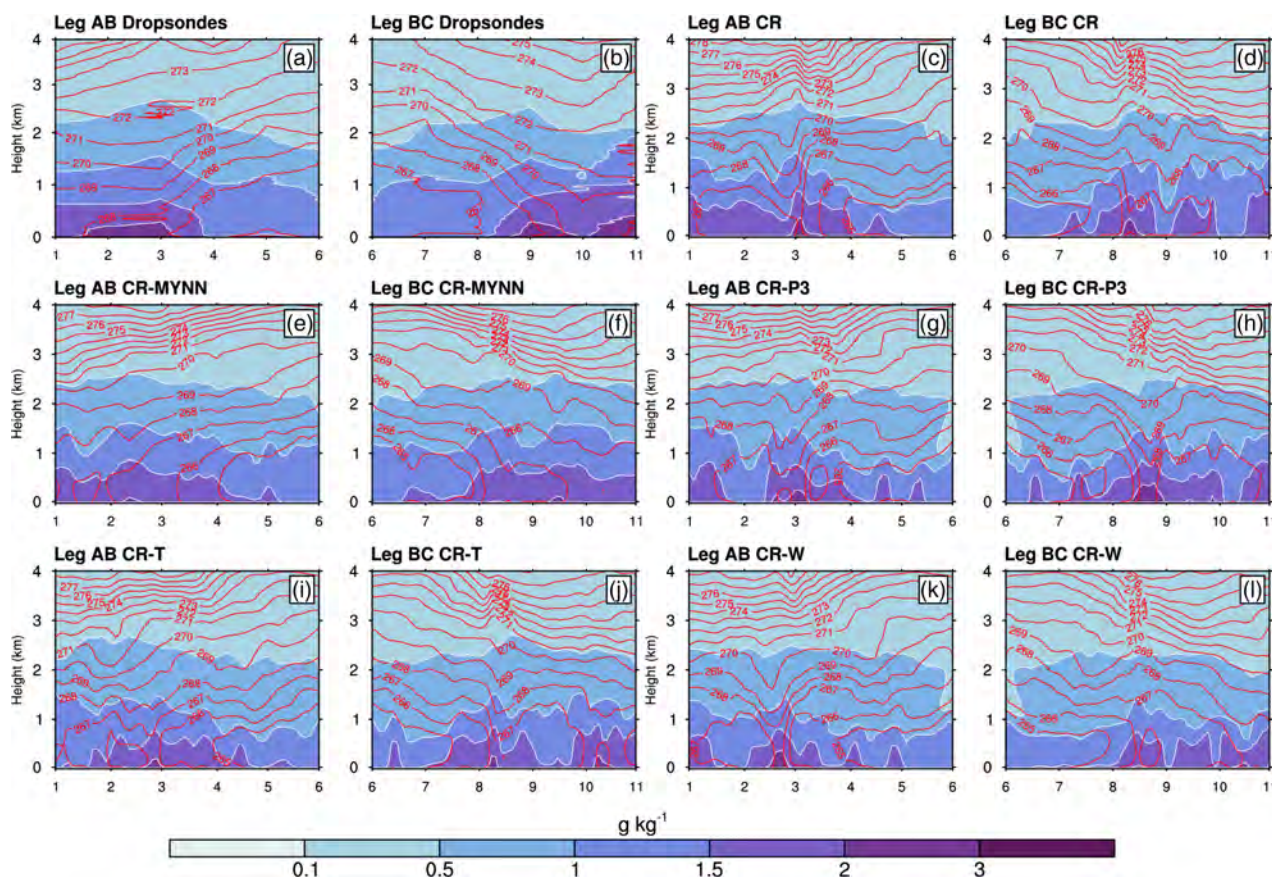


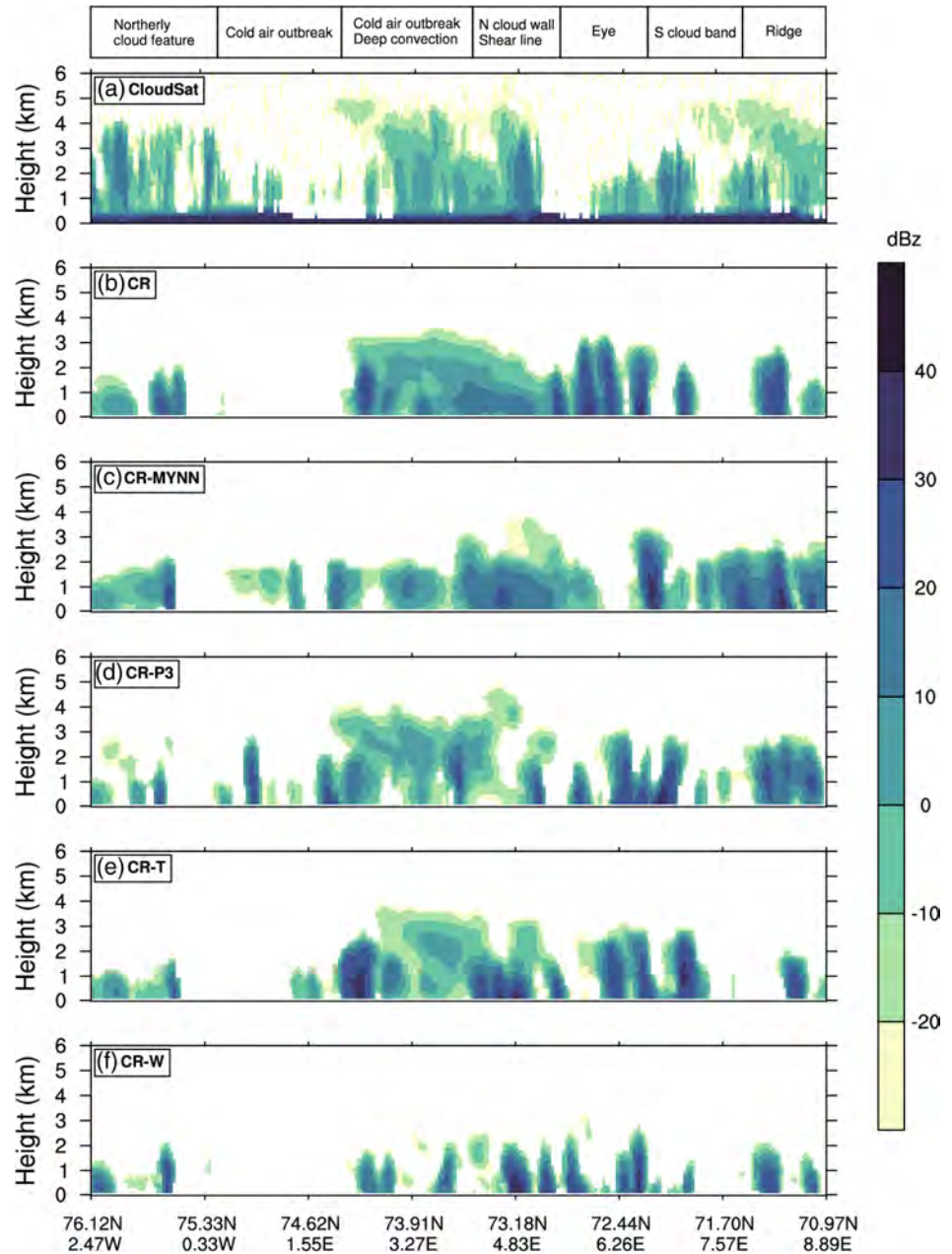
**FIGURE 8** Vertical cross-sections of water vapour mixing ratio (blue colour shading,  $\text{g}\cdot\text{kg}^{-1}$ ) and potential temperature (red contours, K) along with Legs AB and BC from dropsondes and model output at 1130 UTC 26 March (similar to S17). The positions of A, B and C are shown in Figure 6. (a,b) Interpolated dropsonde soundings, Leg AB used dropsondes 1–6, Leg BC used dropsondes 6–11. (c,d) CR, (e,f) CR-MYNN, (g,h) CR-P3, (i,j) CR-T, and (k,l) CR-W. Numbers on the x-axis identify the dropsondes [Colour figure can be viewed at [wileyonlinelibrary.com](http://wileyonlinelibrary.com)]

of the PL. Figure 2c,d display the top-of-atmosphere outgoing long-wave radiation (OLR) with mean sea-level pressures from the model results at 0600 and 1230 UTC, closest in time to the satellite observations. The model cloud band south of Svalbard, with relatively low OLR ( $\sim 140 \text{ W}\cdot\text{m}^{-2}$ ), highlights the deep convection taking place. Furthermore, the modelled intensification of the PL corresponded closely with the satellite imagery patterns (Figure 2a,b). At 0600 UTC, even though the cloud structures did not stand out, the PL centre ( $\sim 74.5^\circ\text{N}$ ,  $5^\circ\text{E}$ ) is clearly resolved by the 1,012 hPa closed centre (Figure 2c) and the closed circulation of the wind streamlines (speeds exceeding  $18 \text{ m}\cdot\text{s}^{-1}$ , Figure 3c). In the next 6 hr, the PL moved slightly southward and intensified (evidenced by the cloud-free centre located at  $\sim 73^\circ\text{N}$ ,  $5^\circ\text{E}$ ), with a pronounced SLP minimum (1,010 hPa) and a well-developed circulation in the wind field.

The lifetime of the PL in our numerical experiments almost agrees with S17. In the early stages, owing to the continuous southward flow of the MCAO, the main cloud band with high relative vorticity (maxima  $10^{-3} \text{ s}^{-1}$ )

was oriented roughly east–west. From 0000 UTC 26 March, these vortices developed into a quasi-axisymmetric cyclonic disturbance with the vorticity band rolling up and smaller waves merging. The instability criterion for PL formation of the temperature difference between the sea surface (SST) and 500 hPa ( $T_{500}$ ) exceeding  $43^\circ\text{C}$  ( $\text{SST} - T_{500}$ ) (e.g., Zahn and von Storch, 2008a; 2008b; Zappa *et al.*, 2014) is met (see Appendix Figure A1). It is more significant at 0200 UTC associated with the increasing radius of the SLP deficit (see Appendix Figure A2). Further development shows the growth of PL is characterized by the vorticity field and maintains a comma cloud band that identifies a PL on satellite imagery. The SLP and wind streamlines suggest that the mature stage was reached at approximately 1300 UTC as the region of low pressure (1,008 hPa, Table 3) reached its minimum and the accompanying strong winds ( $23 \text{ m}\cdot\text{s}^{-1}$ , Table 3) maximized. After 1500 UTC, the PL diminished and started to disintegrate into smaller disturbances which were absorbed into the new, stronger cyclone a few hundred kilometres from the coast of Norway. Based on this overall consistency, this

**FIGURE 9** Cloud radar reflectivity (dBZ) across the polar low core region estimated from CloudSat (following S17) and model outputs at 1130 UTC 26 March: (a) CloudSat, (b) CR, (c) CR-MYNN, (d) CR-P3, (e) CR-T, and (f) CR-W. The swath traversed from southeast to northwest (right to left) during 1132–1134 UTC and is shown in Figure 1. Feature labels at top are taken from S17 [Colour figure can be viewed at [wileyonlinelibrary.com](http://wileyonlinelibrary.com)]



case-study can be confidently discussed in the following sections.

### 3.2 | Sensitivity to model parameter settings

To identify the optimal model settings, it is important to examine whether the simulations reasonably reproduce the case or not. Five typical simulation results of the PL at the mature stage are shown in Figures 4 and 5. For a quantitative estimate, Table 3 shows the minimum SLP, the maximum wind speed at 10 m, the maximum relative vorticity at 950 hPa, the maximum latent-heat flux, the

maximum sensible-heat flux and the minimum SST–T500 that are calculated from the PL region (72–74°N, 2–10°E, box areas shown in Figures 4 and 5), respectively. Verification of the simulations is discussed next.

As mentioned in Section 2.3.2, different experiments explore the impacts of the initial conditions. Compared to Cycling Runs (CR), Cold Start (CS-12) runs did not resolve the PL very well. This was verified by the OLR, SLP and wind field patterns shown in Figures 4a,e and 5a,e. For the CR-NR, the low OLR values (Figure 4c) revealed the convection that successfully matched the cloud structure of the satellite image, but the lack of the minimum SLP centre and a closed vortex in the wind field (Figure 5c) depicted a weaker PL. Also, it had smaller wind speeds,



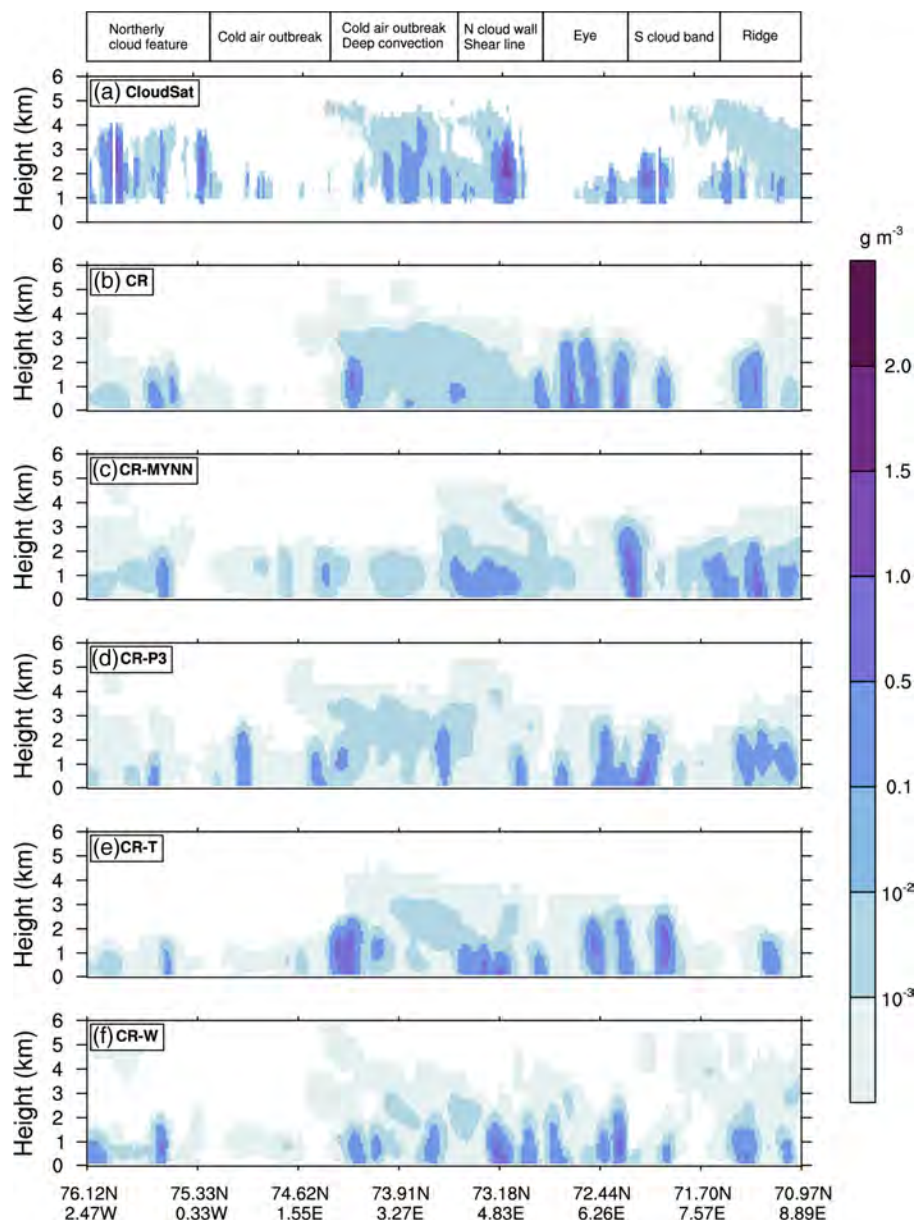


**FIGURE 10** Cloud ice water content (IWC,  $\text{g m}^{-3}$ ) across the polar low core region estimated from CloudSat (following S17) and model outputs at 1130 UTC 26 March: (a) CloudSat, (b) CR, (c) CR-MYNN, (d) CR-P3, (e) CR-T, and (f) CR-W. The swath that passed from southeast to northwest during 1132–1134 UTC is shown in Figure 1. Feature labels at top are taken from S17 [Colour figure can be viewed at [wileyonlinelibrary.com](http://wileyonlinelibrary.com)]

relative vorticity, latent-heat flux and sensible-heat flux than CR (Table 3). This means that the model still faced challenges in capturing the PL without radiance data assimilation.

Because of its small scale, the rapidly developing PL is sensitive to the model's initialization time; Cold Start simulations at 0000 and 1200 UTC on 25 March (25.00 and 25.12) with spin-up time of 24 and 12 hr, respectively (both end at 27.00) were conducted. The Cold Start runs are consistent with the conclusion of S17 that simulations initialized at 25.12 show better performance. But the contrast is not evident in the Cycling Runs.

Previous studies emphasized that high horizontal resolution is a requirement for PL simulations. (e.g., Kristiansen *et al.*, 2011; McInnes *et al.*, 2011; Sergeev *et al.*, 2017; 2018). For WRF, 5 or 3 km horizontal resolution

(inner domain) is believed to be appropriate (e.g., Wu and Petty, 2010; Førre *et al.*, 2012; Kolstad *et al.*, 2016). Here, a single domain with horizontal resolutions of 3, 6 and 9 km were assessed. As 9 km horizontal resolution produced poorer results than 6 km, only the results of 3 km (CR) and 6 km (CR-6 km) are shown. Compared with 3 km, 6 km horizontal resolution usually simulated a weaker PL that indicates 6 km resolution is not fine enough for such a small PL. The snapshots at 1300 UTC are displayed in Figures 4d and 5d. Also, the values given in Table 3 indicate that 6 km is not as good as 3 km.

To maintain the balance between accuracy and variability in grid nudging strategy, a series of tests suggested that switching off nudging for  $T$ ,  $Q$  (specific humidity),  $U$  and  $V$  below model level 35 (roughly 550 hPa) significantly promotes model forecast skill. The

**TABLE 4** Identified PL cases during March 2013 and model performance near mature stage

Time period <sup>a</sup>	Serial number	CR	CR-NR	CS	ASCAT validation	Reference
F: 1 March, 0600 UTC T: 2 March, 0000 UTC	1	Developed	Intermittent	Missing	Y	Figure 11a, row 1
F: 4 March, 0300 UTC T: 5 March, 0300 UTC	2	Developed	Developed	Developed	Y	Figure 11a, row 2
	3	Developed	Intermittent	Missing	Y	
	4	Intermittent	Intermittent	Intermittent	Y	
F: 5 March, 0900 UTC T: 7 March, 0300 UTC	5	Developed	Intermittent	Intermittent	Y	Figure 11a, row 3
	6	Developed	Missing	Intermittent	Y	
F: 11 March, 0900 UTC T: 13 March, 0000 UTC	7	Developed	Intermittent	Missing	Y	Figure 11b, row 1
F: 30 March, 0300 UTC T: 31 March, 0300 UTC	8	Developed	Intermittent	Missing	Y	Figure 11b, row 2
	9	Intermittent	Intermittent	Missing	Y	

<sup>a</sup>Time period: identified duration of each PL corresponding to the time of model output. F,T: indicate the approximate beginning and ending time of satellite signatures, respectively.

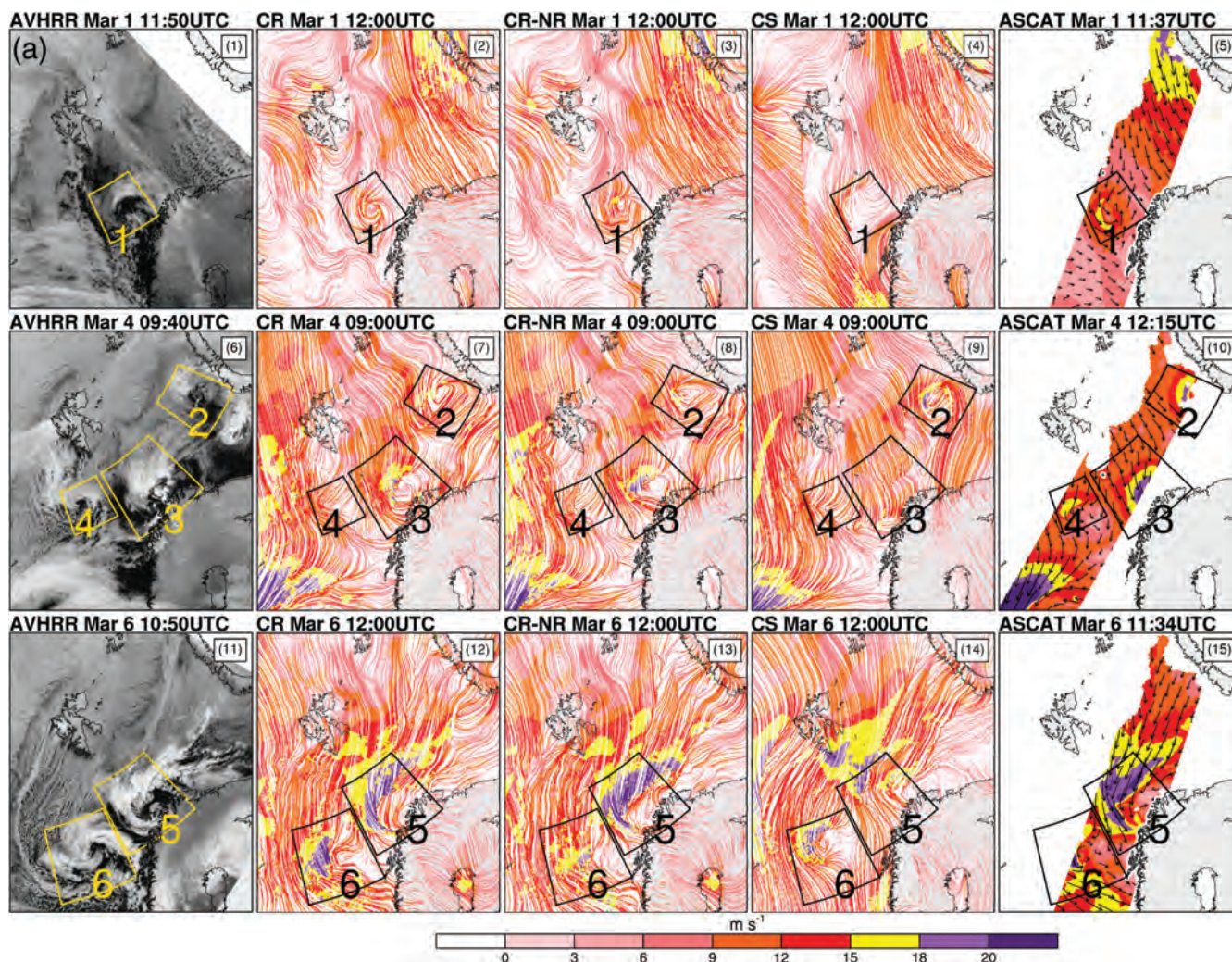


**FIGURE 11** (a) PL cases identified from AVHRR (channel 4) imagery and corresponding model output (wind speed at 10 m plus streamlines,  $\text{m}\cdot\text{s}^{-1}$ ) and surface winds (at 10 m,  $\text{m}\cdot\text{s}^{-1}$ ) from ASCAT at roughly the same time. The first column is the AVHRR imagery and columns two to four are simulations with satellite radiances (CR), without satellite radiances (CR-NR) and PWRP alone (CS), respectively. The boxes with bold numbers indicate the areas of each PL and its serial number. Each panel has an identifying number in the top right. (b) Figure 11 continued [Colour figure can be viewed at [wileyonlinelibrary.com](http://wileyonlinelibrary.com)]



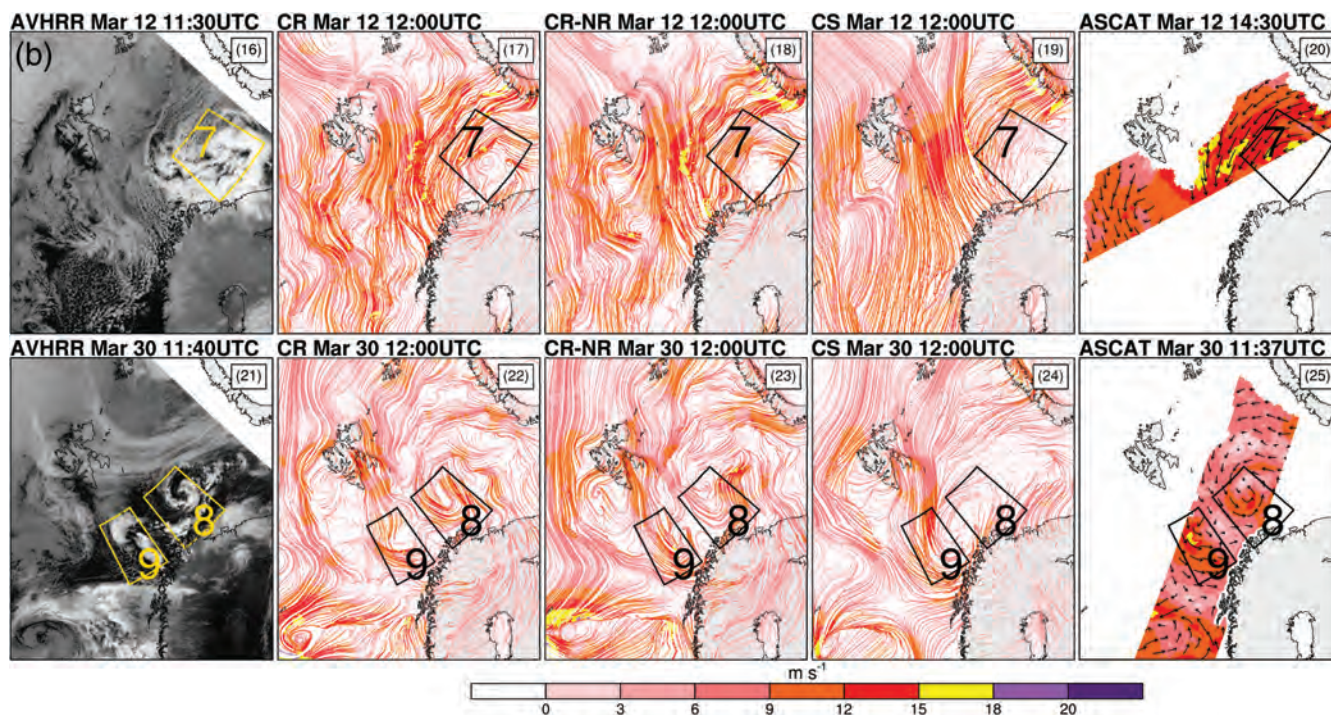


FIGURE 11 Continued [Colour figure can be viewed at [wileyonlinelibrary.com](http://wileyonlinelibrary.com)]

nudging coefficients tested were with the WRF's default strength (0.0003, as strong nudging, CR-NS), a moderate value (0.0001, one-third of default strength, CR) and a weak value (0.00003, approximately one-third of moderate value, CR-NW). The moderate value (0.0001) proved to be the most suitable. This is mainly because weak nudging did not have enough strength to force the model to follow the prescribed large scales while strong nudging could dampen the model's ability to generate important mesoscale features near the surface (Bowden *et al.*, 2012).

The impacts of DFI were also examined. Generally, DFI can reduce and/or eliminate high-frequency features, including the noise of the model's initial state (Peckham *et al.*, 2016). Dolph filter is the default option and recommended by WRF. A more comprehensive description of this is available from Skamarock *et al.* (2019) and the WRF user's guide ([https://www2.mmm.ucar.edu/wrf/users/docs/user\\_guide\\_v4/v4.1/contents.html](https://www2.mmm.ucar.edu/wrf/users/docs/user_guide_v4/v4.1/contents.html)). Here, Dolph filter with the 30 min backward-forward in time was utilized in the simulation (CR-DFI) with other settings the same as the control run (CR). However, not only was the noise removed, but some small-scale unstable systems were also suppressed. As OLR shows in Figure 4b, too many dark patches imply some small convective features or instabilities were lost, especially over the Norwegian Sea (south of the PL). Moreover, the model with DFI produced a smaller maximum wind speed, relative vorticity, latent-heat flux and sensible-heat flux (Table 3).

### 3.3 | Performance of different physical schemes

This section investigates the performance of different PBL and microphysics schemes by combined analysis of ASCAT wind estimates, direct observations from dropsonde profiles, and radar measurements from CloudSat. The model parameter settings used here are the same as the control run (CR) except with different physical schemes. MYNN and MYJ PBLs were investigated by comparing CR-MYNN and CR. Morrison-2-moment with liquid water droplet concentrations of 50, 10 and 100  $\text{cm}^{-3}$  were investigated and only the 50  $\text{cm}^{-3}$  option (CR) is discussed here because it produced the best result. CR-P3, CR-T and CR-W are used to evaluate the P3, aerosol-aware Thompson and WDM6 microphysics schemes, respectively (see Table 2).

#### 3.3.1 | Horizontal structure

As the consistency between the simulations and the satellite imagery has been shown above, here the horizontal structure mainly focuses on the surface wind. At 1300 UTC, the PL transitioned into the mature stage and all the simulations in Figure 6 clearly describe the PL with the well-defined circulation centre to the east of the strong wind region (yellow and purple colour fill). Compared to ASCAT (Figure 6a), the model generally demonstrated a

slightly weaker wind gradient over the main wind zone, but the simulations resolve the core of PL which appears as a relatively calm area (Figure 6). The different physical schemes did not show much effect on the location of the PL, but the difference in the intensity was clear. Also, although MYNN simulated a calm wind centre, the maximum wind speed was lower than observed (Figure 6c). Wind speed, especially the strong wind region (exceeds  $15 \text{ m s}^{-1}$ ) depicted by MYJ with Morrison-2-moment (CR, with liquid water droplet concentrations reduced to  $50 \text{ cm}^{-3}$ ) was found to be closer to the observations.

### 3.3.2 | Vertical structure

The dropsondes released along Legs AB and BC provide two snapshots of the atmospheric vertical profile below 4 km crossing the strong wind zone (the northeast shear line). Therefore, two vertical cross-sections along the flight legs from the southeast (A) to northwest (B) and back to the southeast (C) are shown in Figure 7. The vertical wind profile (Figure 7a,b) presents the sharp horizontal wind gradient that is consistent with ASCAT (Figure 6a). Benefitting from the high-frequency data collected, Figure 7a,b show the low-level jet that is well defined by dropsondes 4 and 9. It sampled the maximum ( $\sim 20 \text{ m s}^{-1}$ ) contour with the speed gradually decreasing outward below 3 km. In general, the simulations roughly capture the main features of the vertical wind structure, but the intensity and position of the jet core are approximate in part because of the displacement of the model low. MYNN (Figure 7e,f) in particular produces a weaker wind field that is consistent with the conclusion discussed in Section 3.3.1. MYJ (CR, Figure 7c,d) captures the core better than MYNN (CR-MYNN, Figure 7e,f) but the speed is still not strong enough. Although the boundary of strong wind zone and calm wind core are clear (dropsondes 4 and 9), the modelled gradient is too sharp and narrow below 1 km. MYJ with Morrison-2-moment (Figure 7c,d) and P3 (Figure 7g,h) best capture the vertical wind structure.

The cross-sections of water vapour mixing ratio (MR, blue filled contour) and potential temperature ( $\theta$ , red lines) along Legs AB and BC are shown in Figure 8. Quantitatively, the results are consistent with studies that claimed the MR in the cloud bands near the PL core probably is  $\sim 2 \text{ g kg}^{-1}$  (e.g., Brümmer *et al.*, 2009; Sergeev *et al.*, 2017). For MYNN (Figure 8e,f), the smooth contours and somewhat low moisture content near the surface suggest weaker instability may be the reason for the lower wind speeds discussed above. For MYJ, the peak of moisture near dropsondes 3 and 9 was captured by Morrison-2-moment (Figure 8c,d) and P3 (Figure 8g,h). However, the many ups and downs of the MR in our

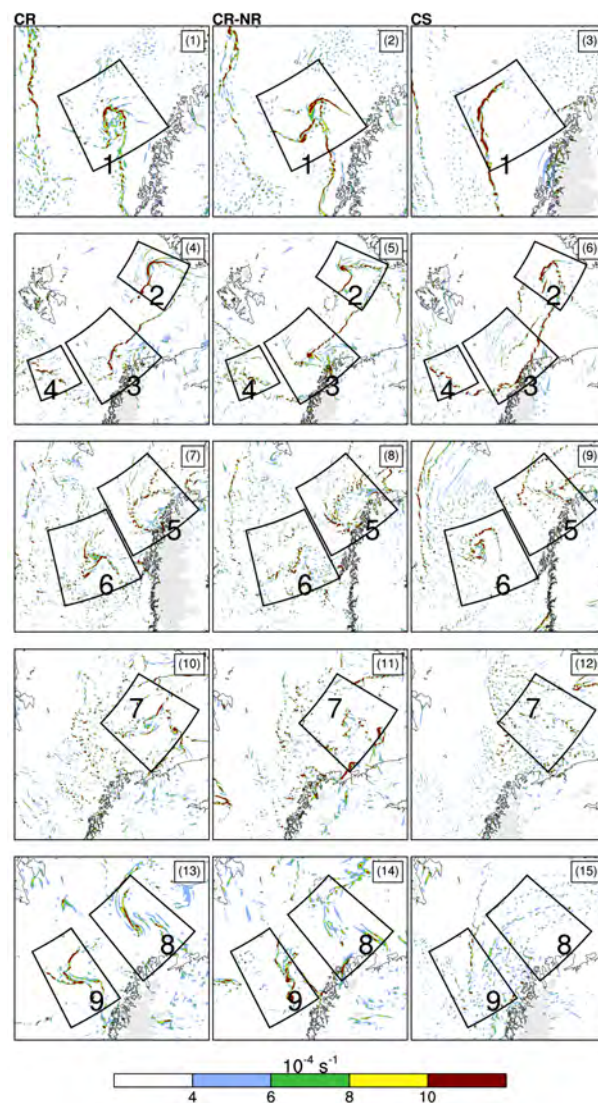


**FIGURE 12** Relative vorticity (colours) at 950 hPa. The columns from left to right are the simulations with satellite radiances (CR), without satellite radiances (CR-NR) and PWRF alone (CS), respectively. The boxes with bold numbers indicate the areas of each PL and its serial number [Colour figure can be viewed at [wileyonlinelibrary.com](http://wileyonlinelibrary.com)]

experiments below  $\sim 1,500 \text{ m}$  hint that several small convective features or instabilities were developing (Figure 8). Analogous undulations are present in the potential temperature field. Moreover,  $\theta$  produced by the model is approximately  $1^\circ \text{C}$  lower below 3 km but higher above, producing greater stability in the model than in the observations. Diagnosis of the cause is beyond the scope of this article.

### 3.3.3 | Cloud

Close to the PL centre, the large-scale vertical cloud structure across the northeasterly strong wind band



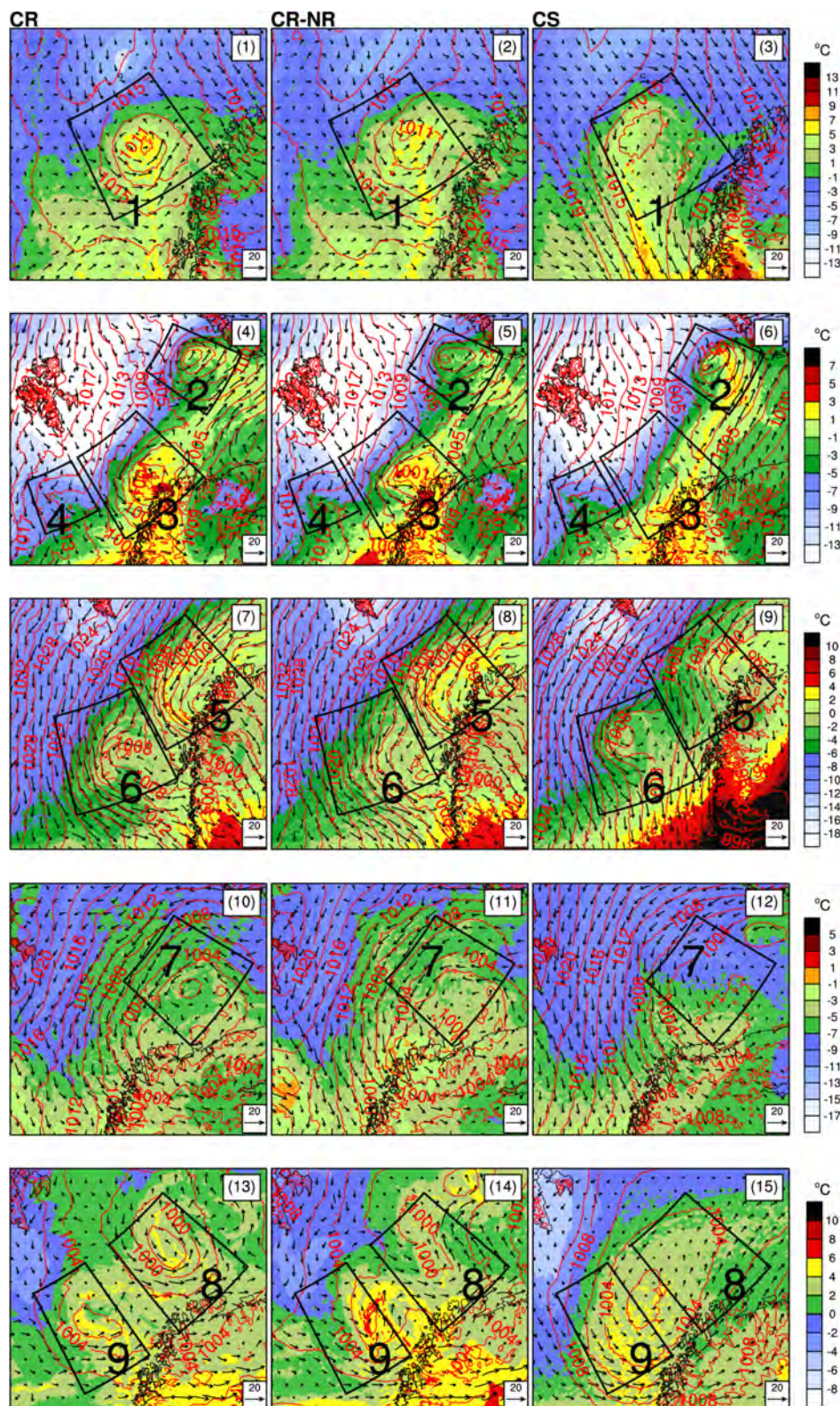


**FIGURE 13** The equivalent potential temperature at 850 hPa (colour shading), wind vector at 850 hPa (black arrows) and the sea-surface pressure (red contours, hPa). The columns from left to right are the simulations with satellite radiances (CR), without satellite radiances (CR-NR) and PWRP alone (CS), respectively. The boxes with bold numbers indicate the areas of each PL and its serial number [Colour figure can be viewed at [wileyonlinelibrary.com](http://wileyonlinelibrary.com)]

was provided by CloudSat. It passed by from southeast to northwest during 1132–1134 UTC (Figure 1). The strong radar echo ( $\sim 20$  dBZ) from CloudSat approximately between  $73.91^{\circ}\text{N}$ ,  $3.27^{\circ}\text{E}$  and  $73.18^{\circ}\text{N}$ ,  $4.83^{\circ}\text{E}$  suggests a region of deep convection with cumulus-type cloud towers

$\sim 4.5$  km tall (Figure 9a). Toward the southeast (right), less active convection is present that could evolve into a calm region (PL eye). At the same time, the other weaker area to the northwest (left, around  $74.62^{\circ}\text{N}$ ,  $1.55^{\circ}\text{E}$ ) indicates the MCAO. Overall, our simulations reasonably approximate



the radar echo patterns produced by CloudSat, considering the demands placed on the model fields for precise positioning as well as the structural differences between the model results and observations south of the PL centre (e.g., Figure 2d compared to Figure 2b). The location and high intensity of convection at the leading edge (eastern) of the MCAO, that indicates latent heat is being released which is fuelling the PL development, is well simulated by CR although the lower height ( $\sim 3.5$  km or less) means convection is shallower as a result of the model's greater stratification aloft than the observations reveal (Figure 8). In general, the modelled convective features in CR show much less structure than CloudSat probably indicating that the model horizontal resolution is not high enough (e.g., Stoll *et al.*, 2020).

The LWC and IWC are evaluated by analysis of CloudSat and simulations with different physical schemes. The LWC is confined to the lowest 2 km with maximum concentration exceeding  $1 \text{ g}\cdot\text{m}^{-3}$  indicated by CloudSat (see Appendix Figure A3). Most LWC estimated from model outputs shows more vertical spread and higher amounts than CloudSat records and are tied to the convective cells revealed by radar echoes except for WDM6 (CR-W) that produces almost no LWC. For different physical schemes, the quantity of LWC shows more sensitivity to the microphysics scheme while the PBL changes the vertical spread more significantly. In summary, the Morrison-2-moment and P3 show a better capability to produce LWC (Appendix Figure A3). Obviously, the clouds are rich in IWC, reaching a peak of  $1.0\text{--}1.5 \text{ g}\cdot\text{m}^{-3}$  at roughly 3 km height estimated from CloudSat (Figure 10). The model indicated consistent values but placed the maximum at a height lower than 3 km except for Morrison-2-moment (CR). In addition, this feature of greater amount of IWC, to some extent, was also noticed by S17. This indicates that the ice phase prevails over the liquid phase in such mixed-phase clouds. Overall, the model shows reasonable skill in representing clouds but maintaining the appropriate balance of LWC and IWC remains a major modelling challenge.

#### 4 | EVALUATION OF MONTH-LONG SIMULATIONS

The PLs that formed during the three month-long simulations introduced in Section 2.3.2 are evaluated here. The refined model parametrizations from the case-study are as follows: 3 km horizontal resolution driven by ERA-Interim, grid nudging with 0.0001 weight, DFI turned off, MYJ and Morrison with  $50 \text{ cm}^{-3}$  liquid water droplet concentrations. That is, reanalysis mode cycling data assimilations using PWRf with 3DVAR were performed with the same settings as CR and CR-NR to assess

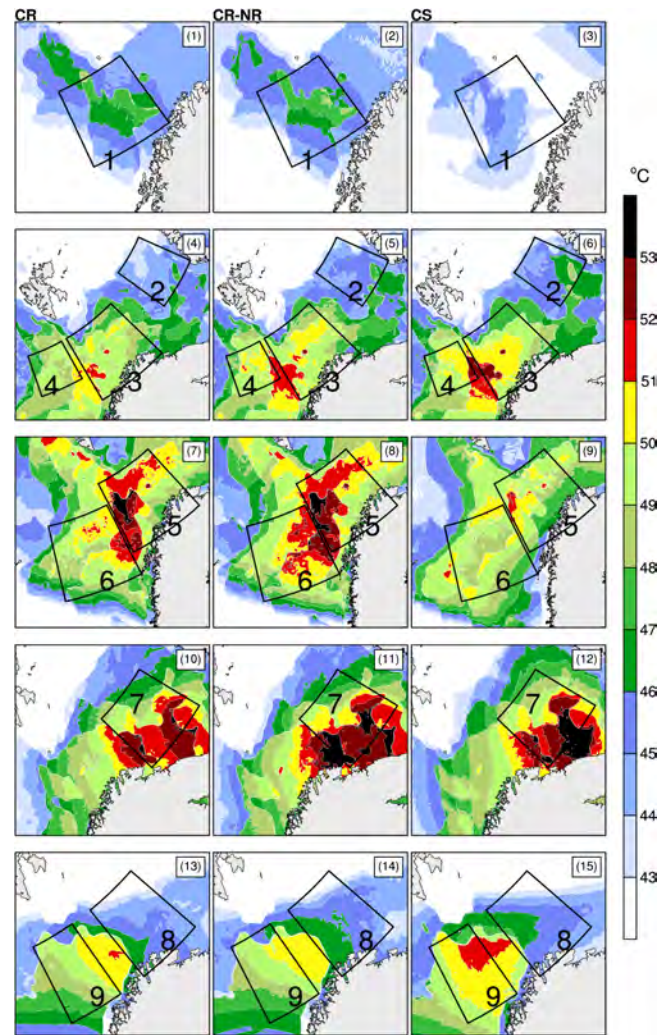


**FIGURE 14** The differences of SST minus T at 500 hPa ( $\text{SST}-\text{T}_{500}$ , colour contour whose values exceed  $43^\circ\text{C}$ ). The columns from left to right are the simulations with satellite radiances (CR), without satellite radiances (CR-NR) and PWRf alone (CS), respectively. The boxes with bold numbers indicate the areas of each PL and its serial number [Colour figure can be viewed at [wileyonlinelibrary.com](http://wileyonlinelibrary.com)]

respectively the capability of continuous assimilation of both synoptic and satellite radiance data versus synoptic observations only. The PWRf-only simulations are cold-started from ERA-Interim. All three runs have 3 hr forecasts to highlight PL simulation sensitivity to the initial conditions. The simulations begin on 0000 UTC 1 March and end at 2100 UTC 31 March with 3-hourly output.

The manual identification of PL is conducted using AVHRR thermal infrared satellite imagery as recommended by other investigators (e.g., Zabolotskikh *et al.*, 2010; Rojo *et al.*, 2015). Although satellite imagery revealed several possible characterizations of cloud signatures associated with PL in previous studies, most PLs



**TABLE 5** The mean and standard deviation of the gridded bias for each PL relative to ASCAT

Time <sup>a</sup>	PLs	Region	CR		CR-NR		CS	
			Mean	Stdv	Mean	Stdv	Mean	Stdv
M: 1 March, 1200 UTC O: 1 March, 1137 UTC	1	70.5–74°N 12–20°E	–1.66	2.40	–0.63	2.62	–4.65	4.53
M: 4 March, 0900 UTC O: 4 March, 1215 UTC	2	72–76°N 40–52°E	–0.29	3.88	–1.20	4.29	–0.54	3.68
	3	70.5–74°N 18–30°E	–0.59	3.90	–0.76	3.44	–3.04	3.13
	4	72–75°N 5–15°E	–1.56	3.35	–0.72	3.17	–0.20	3.46
M: 6 March, 1200 UTC O: 6 March, 1134 UTC	5	70–74.5°N 13.5–28.5°E	0.04	3.08	0.48	3.57	–3.45	4.37
	6	69–74°N 1–13°E	–1.29	3.59	–1.10	3.33	–3.24	3.87
M: 12 March, 1200 UTC O: 12 March, 1214 UTC	7	70–74°N 32–45°E	–1.88	2.36	–3.98	2.34	–5.62	2.64
M: 30 March, 1200 UTC O: 30 March, 1137 UTC	8	70.5–74.5°N 25–35°E	0.85	3.49	–0.96	3.60	–3.12	3.37
	9	70.5–74.5°N 13–21°E	–1.84	3.12	–0.33	3.20	–0.90	2.82
Average			–0.91	3.24	–1.02	3.29	–2.75	3.54

<sup>a</sup>Time, the time of model output and approximate time of ASCAT swath. M, the time of model output. O, the time of ASCAT. Region for each PL using the box area shown in the previous figures (e.g., Figure 14).

examined in this study are spiraliform or comma shaped (e.g., Carleton, 1995; 1996; Rasmussen and Turner, 2003; Rojo *et al.*, 2015). For PLs occurring in pairs or multiple centres on the satellite imagery, each system is recorded in the list. The satellite images are available every 3 hr or less; therefore, there is a gap between each AVHRR observation and model output. The approximate duration of PLs corresponds to the time between the first and last satellite observation which rounds up to every 3 hr. As the cloud structure is displayed more distinctly when the eye is evident or the cloud band strongly curved, the duration of each PL is a minimum focused around its mature stage. Overall, 9 PLs are identified in addition to the case presented by S17 over the Nordic Seas (see Table 4, the first two columns).

To examine the capability of reproducing PLs during a long-term integration, the surface wind (10 m) and sea-level pressure from PWRP alone (CS), PWRP assimilating synoptic observations only (CR-NR) and PWRP assimilating both the synoptic and satellite radiance data (CR) are analysed to identify the PLs. For further comparison of the three month-long simulations, the following model classification is applied: (a) both the surface wind and sea-level pressure usually maintain a

well-defined closed circulation during the PL lifetime, here labelled as “Developed”; (b) intermittently the surface wind and sea-level pressure resolve a closed circulation, labelled as “Intermittent”; and (c) either the surface wind or sea-level pressure generally did not capture the closed circulation, labelled as “Missing”. The statistical results are shown in Table 4. In general, month-long simulations show the ability to simulate PLs. Arriving at the same conclusion as the case-study, it is evident that simulations based on satellite radiances captured characteristics of PLs very well, namely having a well-defined closed circulation both in surface winds and sea-level pressure. For the CR, seven PLs are classified as “Developed” and two PLs are labeled “Intermittent”. However, the model could at times miss small (weak) PLs when simulations do not have satellite radiances to assimilate. There are five cases in the CS simulations and one case in CR-NR marked as “Missing”. These findings demonstrate that CR shows the best performance and CR-NR is better than CS but not nearly as good as CR. In other words, simulation of wind speed and sea-level pressure associated with PLs using the PWRP model is significantly improved by data assimilation and both synoptic data and satellite radiances are required.

The scatterometer winds from ASCAT are used to verify the PLs identified by AVHRR imagery and month-long simulations. Because the time and space coverage of ASCAT is much poorer than AVHRR, measurements of the 10 m wind speed and direction only offer limited comparisons. Fortunately, an orbit passed over nearby areas and at least one image is available for each PL. Figure 11a,b show a typical characterization of the 9 PL cases at their mature stage identified from AVHRR with corresponding surface winds from model output and ASCAT winds at roughly the same time. The AVHRR imagery (channel 4) is plotted in the left column, columns 2–4 are the winds at 10 m from model output of CR, CR-NR and CS, respectively. Ten-metre scatterometer winds from ASCAT are located in the right column. Usually, the spiraliform or comma-shaped white cloud signatures and the strong near-surface winds with a closed circulation or vortex (maximum at least  $15 \text{ m}\cdot\text{s}^{-1}$ ) are present indicating PLs, as summarized in Table 4. However, case 8 has wind speeds that do not reach the PL threshold of  $15 \text{ m}\cdot\text{s}^{-1}$  in ASCAT data (exceeding  $12 \text{ m}\cdot\text{s}^{-1}$ ). A possible reason for this is the PL did not yet reach or has already passed the strongest stage at this time. Simultaneously, the accuracy (better than  $2 \text{ m}\cdot\text{s}^{-1}$ ) and the bias (less than  $0.5 \text{ m}\cdot\text{s}^{-1}$ ) of ASCAT measurements should also be taken into account (Lavergne *et al.*, 2019). Unfortunately, limited observations prevent further analysis.

These findings also are supported by the assessments of specific characteristics of PLs. Figure 12 shows the relative vorticity at 950 hPa from the model output of CR, CR-NR and CS at the same time as displayed in Figure 11a,b (relative vorticity at 850 hPa shows similar results). The following characteristics are obvious. First, PLs that are labelled “Developed” or “Intermittent” usually show quasi-axisymmetric or bending structure with a strong relative vorticity band while those labelled “Missing” do not. For most PLs, CR does the best illustrating the strong relative vorticity band and CS the worst. The conclusions are also supported by the analysis of equivalent potential temperature (Figure 13). For each PL, there is a clear warm core accompanied by a low-pressure centre and a closed circulation in the wind vectors. Moreover, the SST–T500 difference is used to confirm the presence of MCAO in the surroundings. When PLs form, the criterion that SST–T500 exceeds  $43^\circ\text{C}$  is satisfied (Figure 14).

To make the comparison with ASCAT 10 m winds more quantitative, the bias (model output minus ASCAT) of wind speed is calculated as an additional evaluation of the simulated PLs (Table 5). As the time and space coverage of ASCAT is limited for each PL case, only the same swaths that are used for PL verification above are available (shown in Figure 11a,b, right column). Each model output is bilinearly interpolated to the grid points of ASCAT.

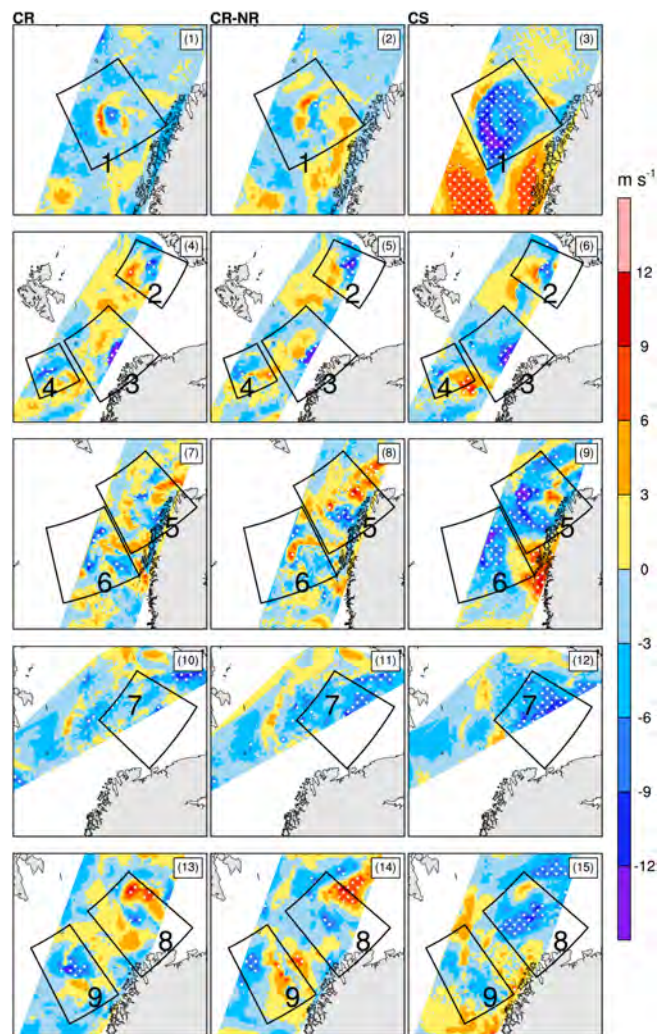


**FIGURE 15** The bias of 10 m wind speed ( $\text{m}\cdot\text{s}^{-1}$ ) calculated from the same model output and ASCAT swaths used for PL verification in Figure 11. The white dots indicate the absolute bias exceeds  $6 \text{ m}\cdot\text{s}^{-1}$ . The columns from left to right are the simulations with satellite radiances (CR), without satellite radiances (CR-NR) and PWRP alone (CS), respectively. The boxes with bold numbers indicate the areas of each PL and its serial number [Colour figure can be viewed at [wileyonlinelibrary.com](http://wileyonlinelibrary.com)]

The spatial distribution of the bias for each ASCAT swath is shown in Figure 15 with white dots indicating that the absolute bias exceeds  $6 \text{ m}\cdot\text{s}^{-1}$ . In summary, the negative bias over the PL centre or over the entire ASCAT swath means that the model is producing weaker winds as has been already shown. The positive bias patches, bending, or quasi-axisymmetric cyclonic, over the PL development region, well matches the cloud pattern shown by AVHRR imagery (Figure 11a,b, left column). This may suggest convection is taking place in the strong wind region surrounding the centre. Two reasons may explain this positive difference. First, the original model output with higher horizontal resolution ( $3 \text{ km}$ ) provides a better convection



description (manifested as higher wind speed) than the 12.5 km ASCAT data. Alternatively, the model may generate too many small-scale unstable systems.

The performances of CR, CR-NR and CS are also revealed by comparing the bias of each PL active area. The well-simulated PL cases verified above (labelled as “Developed” in Table 4) typically show minor bias with the bending or quasi-axisymmetric cyclonic positive bias patches that can be linked to developing convection (Figure 15). On the contrary, the PLs that were not well captured by the model were accompanied by a large negative bias. Undoubtedly, the bias of CR with minimal coverage of white dots not only indicates the best comparison with observation but also illustrates most of the PL cases were well-produced including cases 1, 2, 3, 5, 6, 7 and 8. CR-NR demonstrates comparable results with CR but not as skilful. CS simulations have much bigger negative biases (exceeding  $-9 \text{ m}\cdot\text{s}^{-1}$ ), especially near the PL region, including cases 1, 3, 5, 6, 7 and 8 (see the right column of Figure 15) which are marked as “Missing” or “Intermittent” in Table 4. Table 5 shows the mean and standard deviation of the gridded bias for each PL. The findings discussed above are generally supported by these statistics. The CR runs show a smaller average standard deviation and bias. The CR-NR runs always show similar values to the CR while the CS runs have the largest absolute values. Additionally, most of the means are negative also suggesting weaker winds simulated by the model that is consistent with the previous discussion.

## 5 | SUMMARY AND DISCUSSION

This study focuses on the effects of initial conditions and model configuration on the simulations of PLs using PWRP and WRFDA-3DVAR of synoptic observations and satellite radiances in the vicinity of Svalbard during March 2013. First, the well-documented PL case studied by S17 is re-investigated. The purpose is to investigate the impacts of initial conditions and PWRP configuration on PL simulations using an ensemble of sensitivity experiments with comprehensive remote sensing and *in situ* observations including AVHRR, ASCAT, CloudSat and dropsondes. Then, three month-long simulations of PL formation and development are performed to examine the capabilities for simulating these extreme small-scale phenomena for an extended period: PWRP alone, PWRP assimilating synoptic observations only and PWRP assimilating both synoptic and satellite radiance data with the configurations of Polar WRF and 3DVAR chosen based on the case-study. The validation results using AVHRR, ASCAT satellite data and the analysis of PL characteristics show that the best performance of simulations of PLs is

obtained by cycling data assimilation using both satellite radiances and synoptic data.

The present study reveals that PWRP shows a reasonable capability to reproduce PLs, and the high-resolution initial conditions for PL simulation are most important. Assimilation of satellite radiances plays a critical role due to the sparse coverage of synoptic observations over the ice-free ocean.

The following conclusions emerge from the sensitivity experiments combined with the month-long simulations. First, PL simulations are very sensitive to initial conditions and are sensitive to the model's initialization time. The case-study agrees with S17 that better results are obtained when the model is cold-started at 1200 UTC 25 March instead of 0000 UTC 25 March. The PL simulations using PWRP only for the month-long run are sensitive to the initialization time and can simulate only some of the PLs. Cycling data assimilation assimilates the observations every 3 hr and provides high-resolution initial conditions to the Polar WRF forecasts to improve the PL predictions. This was also confirmed by the month-long simulations.

Second, in agreement with previous investigations (e.g., Kristiansen *et al.*, 2011; Sergeev *et al.*, 2017; 2018), the forecast model resolution is very important. PLs are well simulated by high-resolution numerical experiments especially at the initial time when the scale of PLs is very small. Finer than 3 km convection-permitting model resolution is recommended. Use of 6 and 9 km resolution with and without data assimilation did not well characterize the PL in our case-study.

Third, nudging and DFI were preliminarily tested in the case-study. Moderate analysis nudging is used by PWRP forecast simulations and cycling data assimilations to prevent the simulations from drifting away from large-scale driving fields and to improve PL simulations especially for the PL locations. Based on the effects of nudging strength stressed by other investigators, a series of sensitivity experiments indicated that the best results are obtained by moderate grid nudging with 0.0001 weight. DFI should be used carefully because it smoothes the initial fields too much to produce PLs when removing the noise of the model's initial state. Additional investigations are required to optimize DFI for PL simulations.

Fourth, the options of different physics schemes show some impacts on the location of the PL development, but the differences in structure and cloud are notable. Both MYNN and MYJ PBL schemes can well simulate the wind field and convection development of the PL, and MYJ shows better performance because MYNN is more suitable for stable boundary layers whereas MYJ is suitable for convective boundary layers. More variation is found from the different microphysics schemes, especially for cloud prediction. In general, the Morrison-2-moment with liquid

water droplet concentrations specified at  $50\text{ cm}^{-3}$  and the P3 scheme show better performance. The aerosol-aware Thompson has comparable results and good skills for simulating LWC. WDM6 shows reasonable results for other fields but does poorly in producing LWC. This is probably because its single-moment parametrization for ice crystals is responsible for its lesser ability to model supercooled liquid water clouds (Listowski and Lachlan-Cope, 2017).

The impact of using high-resolution regional reanalysis as initial conditions instead of global reanalyses is another interesting question. In particular, the performance of WRF-derived products such as the Arctic System Reanalysis for cold-start simulations should be evaluated in the future.

This study also extends the findings of model shortcomings. The convection in our case-study is too shallow as depicted by radar echoes with a lower height (Section 3.3.3, Figure 9). It is more significant for Cycling Runs. One possible explanation is that the analysis–forecast method may not give the model enough freedom or time to fully develop convection. Also, the model's stronger stratification above 3 km than shown in the observations may limit vertical development of convective towers. However, these hypotheses need more investigation.

To summarize, notwithstanding the unavoidable ambiguities, simulations of PLs using PWRP and WRF 3DVAR can capture PLs successfully and reliably simulate them in long-term integrations. The high-resolution initial condition for PL simulation is most important and an optimal forecast model configuration can improve the simulation performance. Moreover, our study provides appropriate model settings for extended PWRP simulations of PLs, and the month-long simulations of PL formation and development demonstrate the model's skill in simulating these extreme small-scale phenomena.

## AUTHOR CONTRIBUTIONS

**Jianjun Xue:** Data curation; formal analysis; investigation; methodology; software; validation; visualization; writing – original draft; writing – review and editing.

**David Bromwich:** Conceptualization; formal analysis; funding acquisition; investigation; methodology; project administration; resources; supervision; validation; visualization; writing – original draft; writing – review and editing.

**Ziniu Xiao:** Conceptualization; formal analysis; funding acquisition; investigation; methodology; project administration; resources; supervision; writing – review and editing. **Le-Sheng Bai:** Conceptualization; data curation; formal analysis; investigation; methodology; software; validation; visualization; writing; original draft; writing – review and editing.

## ACKNOWLEDGEMENTS

This research was supported by Office of Naval Research (ONR) grant N00014-18-1-2361 to the second author. The first author was supported by the Chinese Academy of Sciences, Grant XDA20060501 and Natural Science Foundation of China (NSFC) Grant 91937000. We are grateful to the Facility for Airborne Atmospheric Measurements (FAAM, <https://old.faam.ac.uk/index.php>) for the successful operations during the ACCACIA campaign, and processing and provision of the airborne data analysed here. We also thank the CloudSat Data Processing Center for the CloudSat data (<https://cloudsat.atmos.colostate.edu/data>). We appreciate use of AVHRR data and ASCAT ocean wind vector data that were downloaded from EUMETSAT (<https://www.eumetsat.int/>). The comments from the three reviewers substantially improved the article. Contribution 1611 of Byrd Polar and Climate Research Center.

## ORCID

David H. Bromwich  <https://orcid.org/0000-0003-4608-8071>

## REFERENCES

- Adakudlu, M. and Barstad, I. (2011) Impacts of the ice-cover and sea-surface temperature on a polar low over the Nordic seas: a numerical case study. *Quarterly Journal of the Royal Meteorological Society*, 137(660), 1716–1730. <https://doi.org/10.1002/qj.856>.
- Barker, D., Huang, X.-Y., Liu, Z., Auligné, T., Zhang, X., Rugg, S., Ajjaji, R., Bourgeois, A., Bray, J., Chen, Y., Demirtas, M., Guo, Y.-R., Henderson, T., Huang, W., Lin, H.-C., Michalakes, J., Rizvi, S. and Zhang, X.Y. (2012) The Weather Research and Forecasting model's community variational/ensemble data assimilation system: WRFDA. *Bulletin of the American Meteorological Society*, 93, 831–843. <https://doi.org/10.1175/BAMS-D-11-00167.1>.
- Barker, D.M., Huang, W., Guo, Y.-R., Bourgeois, A.J. and Xiao, Q.N. (2004) A three-dimensional variational data assimilation system for MM5: implementation and initial results. *Monthly Weather Review*, 132, 897–914. [https://doi.org/10.1175/1520-0493\(2004\)132<0897:ATVDAS>2.0.CO;2](https://doi.org/10.1175/1520-0493(2004)132<0897:ATVDAS>2.0.CO;2).
- Bowden, J.H., Otte, T.L., Nolte, C.G. and Otte, M.J. (2012) Examining interior grid nudging techniques using two-way nesting in the WRF model for regional climate modeling. *Journal of Climate*, 25, 2805–2823. <https://doi.org/10.1175/JCLI-D-11-00167.1>.
- Bromwich, D.H., Hines, K.M. and Bai, L. (2009) Development and testing of polar weather research and forecasting model: 2. Arctic Ocean. *Journal of Geophysical Research*, 114(D8). <https://doi.org/10.1029/2008JD010300>.
- Bromwich, D.H., Otieno, F.O., Hines, K.M., Manning, K.W. and Shilo, E. (2013) Comprehensive evaluation of polar weather research and forecasting model performance in the Antarctic. *Journal of Geophysical Research: Atmospheres*, 118, 274–292. <https://doi.org/10.1029/2012JD018139>.
- Bromwich, D.H., Wilson, A.B., Bai, L., Liu, Z., Barlage, M., Shih, C.-F., Maldonado, S., Hines, K.M., Wang, S.-H., Woollen, J.,



- Kuo, B., Lin, H.-C., Wee, T.-K., Serreze, M.C. and Walsh, J.E. (2018) The Arctic System Reanalysis, version 2. *Bulletin of the American Meteorological Society*, 99, 805–828. <https://doi.org/10.1175/BAMS-D-16-0215.1>.
- Bromwich, D.H., Wilson, A.B., Bai, L.-S., Moore, G.W.K. and Bauer, P. (2016) A comparison of the regional Arctic System Reanalysis and the global ERA-Interim Reanalysis for the Arctic. *Quarterly Journal of the Royal Meteorological Society*, 142(695), 644–658. <https://doi.org/10.1002/qj.2527>.
- Brümmer, B., Müller, G. and Noer, G. (2009) A polar low pair over the Norwegian Sea. *Monthly Weather Review*, 137, 2559–2575. <https://doi.org/10.1175/2009MWR2864.1>.
- Carleton, A.M. (1995) On the interpretation and classification of mesoscale cyclones from satellite infrared imagery. *International Journal of Remote Sensing*, 16, 2457–2485. <https://doi.org/10.1080/01431169508954569>.
- Carleton, A.M. (1996) Satellite climatological aspects of cold air mesocyclones in the Arctic and Antarctic. *Global Atmosphere and Ocean System*, 5, 1–42.
- Cha, D.-H., Jin, C.-S., Lee, D.-K. and Kuo, Y.-H. (2011) Impact of intermittent spectral nudging on regional climate simulation using Weather Research and Forecasting model. *Journal of Geophysical Research*, 116(D10). <https://doi.org/10.1029/2010JD015069>.
- Claremar, B., Obleitner, F., Reijmer, C., Pohjola, V., Waxegård, A., Karner, F. and Rutgersson, A. (2012) Applying a mesoscale atmospheric model to Svalbard glaciers [WWW Document]. *Advances in Meteorology*, 2012, 1–22. <https://doi.org/10.1155/2012/321649>.
- Dee, D.P., Uppala, S.M., Simmons, A.J., Berrisford, P., Poli, P., Kobayashi, S., Andrae, U., Balmaseda, M.A., Balsamo, G., Bauer, P., Bechtold, P., Beljaars, A.C.M., van de Berg, L., Bidlot, J., Bormann, N., Delsol, C., Dragani, R., Fuentes, M., Geer, A.J., Haimberger, L., Healy, S.B., Hersbach, H., Hólm, E.V., Isaksen, I., Kållberg, P., Köhler, M., Matricardi, M., McNally, A.P., Monge-Sanz, B.M., Morcrette, J.-J., Park, B.-K., Peubey, C., de Rosnay, P., Tavolato, C., Thépaut, J.-N. and Vitart, F. (2011) The ERA-Interim reanalysis: configuration and performance of the data assimilation system. *Quarterly Journal of the Royal Meteorological Society*, 137(656), 553–597. <https://doi.org/10.1002/qj.828>.
- Ek, M.B., Mitchell, K.E., Lin, Y., Rogers, E., Grunmann, P., Koren, V., Gayno, G. and Tarpley, J.D. (2003) Implementation of Noah land surface model advances in the National Centers for Environmental Prediction operational mesoscale Eta model. *Journal of Geophysical Research*, 108(D22). <https://doi.org/10.1029/2002JD003296>.
- Føre, I., Kristjánsson, J.E., Kolstad, E.W., Bracegirdle, T.J., Saetra, Ø. and Røsting, B. (2012) A ‘hurricane-like’ polar low fuelled by sensible heat flux: high-resolution numerical simulations. *Quarterly Journal of the Royal Meteorological Society*, 138(666), 1308–1324. <https://doi.org/10.1002/qj.1876>.
- Furevik, B.R., Schyberg, H., Noer, G., Tveter, F. and Röhrs, J. (2015) ASAR and ASCAT in polar low situations. *Journal of Atmospheric and Oceanic Technology*, 32, 783–792. <https://doi.org/10.1175/JTECH-D-14-00154.1>.
- Glisan, J.M., Gutowski, W.J., Cassano, J.J. and Higgins, M.E. (2012) Effects of spectral nudging in WRF on Arctic temperature and precipitation simulations. *Journal of Climate*, 26, 3985–3999. <https://doi.org/10.1175/JCLI-D-12-00318.1>.
- Hallerstig, M., Magnusson, L., Kolstad, E.W. and Mayer, S. (2021) How grid-spacing and convection representation affected the wind speed forecasts of four polar lows. *Quarterly Journal of the Royal Meteorological Society*, 147(734), 150–165. <https://doi.org/10.1002/qj.3911>.
- Heidinger, A.K., Foster, M.J., Walther, A. and Zhao, X. (2014) The pathfinder atmospheres–extended AVHRR climate dataset. *Bulletin of the American Meteorological Society*, 95, 909–922. <https://doi.org/10.1175/BAMS-D-12-00246.1>.
- Hines, K.M. and Bromwich, D.H. (2008) Development and testing of Polar Weather Research and Forecasting (WRF) model. Part I: Greenland ice sheet meteorology. *Monthly Weather Review*, 136, 1971–1989. <https://doi.org/10.1175/2007MWR2112.1>.
- Hines, K.M. and Bromwich, D.H. (2017) Simulation of late summer Arctic clouds during ASCOS with Polar WRF. *Monthly Weather Review*, 145, 521–541. <https://doi.org/10.1175/MWR-D-16-0079.1>.
- Hines, K.M., Bromwich, D.H., Bai, L., Bitz, C.M., Powers, J.G. and Manning, K.W. (2015) Sea ice enhancements to Polar WRF. *Monthly Weather Review*, 143, 2363–2385. <https://doi.org/10.1175/MWR-D-14-00344.1>.
- Hines, K.M., Bromwich, D.H., Bai, L.-S., Barlage, M. and Slater, A.G. (2011) Development and testing of Polar WRF. Part III: Arctic land. *Journal of Climate*, 24, 26–48. <https://doi.org/10.1175/2010JCLI3460.1>.
- Hines, K.M., Bromwich, D.H., Wang, S.-H., Silber, I., Verlinde, J. and Lubin, D. (2019) Microphysics of summer clouds in central West Antarctica simulated by the Polar Weather Research and Forecasting model (WRF) and the Antarctic Mesoscale Prediction System (AMPS). *Atmospheric Chemistry and Physics*, 19, 12431–12454. <https://doi.org/10.5194/acp-19-12431-2019>.
- Huang, X.-Y., Xiao, Q., Barker, D.M., Zhang, X., Michalakes, J., Huang, W., Henderson, T., Bray, J., Chen, Y., Ma, Z., Dudhia, J., Guo, Y., Zhang, X.Y., Won, D.-J., Lin, H.-C. and Kuo, Y.-H. (2009) Four-dimensional variational data assimilation for WRF: formulation and preliminary results. *Monthly Weather Review*, 137, 299–314. <https://doi.org/10.1175/2008MWR2577.1>.
- Iacono, M.J., Delamere, J.S., Mlawer, E.J., Shephard, M.W., Clough, S.A. and Collins, W.D. (2008) Radiative forcing by long-lived greenhouse gases: calculations with the AER radiative transfer models. *Journal of Geophysical Research*, 113(D13). <https://doi.org/10.1029/2008JD009944>.
- Iversen, T. (2013) Polar lows - a challenge for predicting extreme polar weather. In: ECMWF WWRP/THORPEX Workshop on polar prediction, 24–27 June 2013, p. 14.
- Janjić, Z.I. (1994) The step-mountain eta coordinate model: further developments of the convection, viscous sublayer, and turbulence closure schemes. *Monthly Weather Review*, 122, 927–945. [https://doi.org/10.1175/1520-0493\(1994\)122<0927:TSMECM>2.0.CO;2](https://doi.org/10.1175/1520-0493(1994)122<0927:TSMECM>2.0.CO;2).
- Kain, J.S. (2004) The Kain–Fritsch convective parameterization: an update. *Journal of Applied Meteorology*, 43, 170–181. [https://doi.org/10.1175/1520-0450\(2004\)043<0170:TKCPAU>2.0.CO;2](https://doi.org/10.1175/1520-0450(2004)043<0170:TKCPAU>2.0.CO;2).
- Kilpeläinen, T., Vihma, T., Laflamme, H. and Karlsson, P.E. (2011) Modelling of spatial variability and topographic effects over Arctic fjords in Svalbard. *Tellus A*, 63, 223–237. <https://doi.org/10.1111/j.1600-0870.2010.00481.x>.
- Kim, D.-H., Kim, H.M. and Hong, J. (2019) Evaluation of wind forecasts over Svalbard using the high-resolution Polar WRF

- with 3DVAR. *Arctic, Antarctic, and Alpine Research*, 51, 471–489. <https://doi.org/10.1080/15230430.2019.1676939>.
- Kolstad, E.W. (2006) A new climatology of favourable conditions for reverse-shear polar lows. *Tellus A*, 58, 344–354. <https://doi.org/10.1111/j.1600-0870.2006.00171.x>.
- Kolstad, E.W. (2011) A global climatology of favourable conditions for polar lows. *Quarterly Journal of the Royal Meteorological Society*, 137(660), 1749–1761. <https://doi.org/10.1002/qj.888>.
- Kolstad, E.W. (2015) Extreme small-scale wind episodes over the Barents Sea: when, where and why? *Climate Dynamics*, 45, 2137–2150. <https://doi.org/10.1007/s00382-014-2462-4>.
- Kolstad, E.W. and Bracegirdle, T.J. (2017) Sensitivity of an apparently hurricane-like polar low to sea-surface temperature. *Quarterly Journal of the Royal Meteorological Society*, 143(703), 966–973. <https://doi.org/10.1002/qj.2980>.
- Kolstad, E.W., Bracegirdle, T.J. and Zahn, M. (2016) Re-examining the roles of surface heat flux and latent heat release in a “hurricane-like” polar low over the Barents Sea. *Journal of Geophysical Research: Atmospheres*, 121, 7853–7867. <https://doi.org/10.1002/2015JD024633>.
- Kristiansen, J., Sørland, S.L., Iversen, T., Bjørge, D. and Koltzow, M.Ø. (2011) High-resolution ensemble prediction of a polar low development. *Tellus A*, 63, 585–604. <https://doi.org/10.1111/j.1600-0870.2010.00498.x>.
- Kristjánsson, J.E., Barstad, I., Aspelien, T., Føre, I., Godøy, Ø., Hov, Ø., Irvine, E., Iversen, T., Kolstad, E.W., Nordeng, T.E., McInnes, H., Randriamampianina, R., Reuder, J., Saetra, Ø., Shapiro, M., Spengler, T. and Ólafsson, H. (2011) The Norwegian IPY–THORPEX: polar lows and Arctic fronts during the 2008 Andøya campaign. *Bulletin of the American Meteorological Society*, 92, 1443–1466. <https://doi.org/10.1175/2011BAMS2901.1>.
- Landgren, O.A., Seierstad, I.A. and Iversen, T. (2019) Projected future changes in marine cold-air outbreaks associated with polar lows in the northern North-Atlantic Ocean. *Climate Dynamics*, 53, 2573–2585. <https://doi.org/10.1007/s00382-019-04642-2>.
- Lavergne, T., Sørensen, A.M., Kern, S., Tonboe, R., Notz, D., Aaboe, S., Bell, L., Dybkjær, G., Eastwood, S., Gabarro, C., Heygster, G., Killie, M.A., Kreiner, M.B., Lavelle, J., Saldo, R., Sandven, S. and Pedersen, L.T. (2019) Version 2 of the EUMETSAT OSI SAF and ESA CCI sea-ice concentration climate data records. *The Cryosphere*, 13, 49–78. <https://doi.org/10.5194/tc-13-49-2019>.
- Lim, K.-S.S. and Hong, S.-Y. (2009) Development of an effective double-moment cloud microphysics scheme with prognostic cloud condensation nuclei (CCN) for weather and climate models. *Monthly Weather Review*, 138, 1587–1612. <https://doi.org/10.1175/2009MWR2968.1>.
- Listowski, C. and Lachlan-Cope, T. (2017) The microphysics of clouds over the Antarctic Peninsula – Part 2: Modelling aspects within Polar WRF. *Atmospheric Chemistry and Physics*, 17, 10195–10221. <https://doi.org/10.5194/acp-17-10195-2017>.
- Liu, P., Tsimpidi, A.P., Hu, Y., Stone, B., Russell, A.G. and Nenes, A. (2012) Differences between downscaling with spectral and grid nudging using WRF. *Atmospheric Chemistry and Physics*, 12, 3601–3610. <https://doi.org/10.5194/acp-12-3601-2012>.
- Mallet, P.-E., Claud, C., Cassou, C., Noer, G. and Kodera, K. (2013) Polar lows over the Nordic and Labrador Seas: synoptic circulation patterns and associations with North Atlantic–Europe wintertime weather regimes. *Journal of Geophysical Research: Atmospheres*, 118, 2455–2472. <https://doi.org/10.1002/jgrd.50246>.
- McInnes, H., Kristiansen, J., Kristjánsson, J.E. and Schyberg, H. (2011) The role of horizontal resolution for polar low simulations. *Quarterly Journal of the Royal Meteorological Society*, 137(660), 1674–1687. <https://doi.org/10.1002/qj.849>.
- Milbrandt, J.A. and Morrison, H. (2015) Parameterization of cloud microphysics based on the prediction of bulk ice particle properties. Part III: Introduction of multiple free categories. *Journal of the Atmospheric Sciences*, 73, 975–995. <https://doi.org/10.1175/JAS-D-15-0204.1>.
- Montgomery, M.T. and Farrell, B.F. (1992) Polar low dynamics. *Journal of the Atmospheric Sciences*, 49, 2484–2505. [https://doi.org/10.1175/1520-0469\(1992\)049<2484:PLD>2.0.CO;2](https://doi.org/10.1175/1520-0469(1992)049<2484:PLD>2.0.CO;2).
- Morrison, H. and Milbrandt, J.A. (2014) Parameterization of cloud microphysics based on the prediction of bulk ice particle properties. Part I: Scheme description and idealized tests. *Journal of the Atmospheric Sciences*, 72, 287–311. <https://doi.org/10.1175/JAS-D-14-0065.1>.
- Müller, M., Batrak, Y., Kristiansen, J., Koltzow, M.A.Ø., Noer, G. and Korosov, A. (2017) Characteristics of a convective-scale weather forecasting system for the European Arctic. *Monthly Weather Review*, 145, 4771–4787. <https://doi.org/10.1175/MWR-D-17-0194.1>.
- Noer, G., Saetra, Ø., Lien, T. and Gusdal, Y. (2011) A climatological study of polar lows in the Nordic Seas. *Quarterly Journal of the Royal Meteorological Society*, 137(660), 1762–1772. <https://doi.org/10.1002/qj.846>.
- Olson, J.B., Kenyon, J.S., Angevine, W.A., Brown, J.M., Pagowski, M. and Sušelj, K. (2019) *A description of the MYNN-EDMF scheme and the coupling to other components in WRF-ARW*. NOAA Technical Memorandum OAR GSD, 61. <https://doi.org/10.25923/n9wm-be49>.
- Otte, T.L., Nolte, C.G., Otte, M.J. and Bowden, J.H. (2012) Does nudging squelch the extremes in regional climate modeling? *Journal of Climate*, 25, 7046–7066. <https://doi.org/10.1175/JCLI-D-12-00048.1>.
- Peckham, S.E., Smirnova, T.G., Benjamin, S.G., Brown, J.M. and Kenyon, J.S. (2016) Implementation of a digital filter initialization in the WRF model and its application in the Rapid Refresh. *Monthly Weather Review*, 144, 99–106. <https://doi.org/10.1175/MWR-D-15-0219.1>.
- Powers, J.G., Manning, K.W., Bromwich, D.H., Cassano, J.J. and Cayette, A.M. (2012) A decade of Antarctic science support through AMPS. *Bulletin of the American Meteorological Society*, 93, 1699–1712. <https://doi.org/10.1175/BAMS-D-11-00186.1>.
- Radovan, A., Crewell, S., Knudsen, E.M. and Rinke, A. (2019) Environmental conditions for polar low formation and development over the Nordic Seas: study of January cases based on the Arctic System Reanalysis. *Tellus A*, 71, 1618131. <https://doi.org/10.1080/16000870.2019.1618131>.
- Rasmussen, E.A. and Turner, J. (Eds.). (2003) *Polar Lows: Mesoscale weather systems in the polar regions*. Cambridge, UK: Cambridge University Press.
- Rojo, M., Claud, C., Mallet, P.-E., Noer, G., Carleton, A.M. and Vicomte, M. (2015) Polar low tracks over the Nordic Seas: a 14-winter climatic analysis. *Tellus A*, 67, 24660. <https://doi.org/10.3402/tellusa.v67.24660>.
- Sergeev, D., Renfrew, I.A. and Spengler, T. (2018) Modification of polar low development by orography and sea ice. *Monthly Weather Review*, 146, 3325–3341. <https://doi.org/10.1175/MWR-D-18-0086.1>.



- Sergeev, D.E., Renfrew, I.A., Spengler, T. and Dorling, S.R. (2017) Structure of a shear-line polar low. *Quarterly Journal of the Royal Meteorological Society*, 143(702), 12–26. <https://doi.org/10.1002/qj.2911>.
- Skamarock, W.C., Klemp, J.B., Dudhia, J., Gill, D.O., Liu, Z., Berner, J., Wang, W., Powers, J.G., Duda, M., Barker, D.M. and Huang, X.-Y. (2019) A description of the Advanced Research WRF Model Version 4 (No. NCAR/TN-556+STR). <https://doi.org/10.5065/1dfh-6p97>.
- Smirnova, J. and Golubkin, P. (2017) Comparing polar lows in atmospheric reanalyses: Arctic System Reanalysis versus ERA-Interim. *Monthly Weather Review*, 145, 2375–2383. <https://doi.org/10.1175/MWR-D-16-0333.1>.
- Smirnova, J.E., Golubkin, P.A., Bobylev, L.P., Zabolotskikh, E.V. and Chapron, B. (2015) Polar low climatology over the Nordic and Barents seas based on satellite passive microwave data. *Geophysical Research Letters*, 42, 5603–5609. <https://doi.org/10.1002/2015GL063865>.
- Stephens, G.L., Vane, D.G., Boain, R.J., Mace, G.G., Sassen, K., Wang, Z., Illingworth, A.J., O'Connor, E.J., Rossow, W.B., Durden, S.L., Miller, S.D., Austin, R.T., Benedetti, A. and Mitrescu, C. (2002) The CloudSat mission and the A-Train: a new dimension of space-based observations of clouds and precipitation. *Bulletin of the American Meteorological Society*, 83, 1771–1790. <https://doi.org/10.1175/BAMS-83-12-1771>.
- Stoll, P.J., Graversen, R.G., Noer, G. and Hodges, K. (2018) An objective global climatology of polar lows based on reanalysis data. *Quarterly Journal of the Royal Meteorological Society*, 144(716), 2099–2117. <https://doi.org/10.1002/qj.3309>.
- Stoll, P.J., Valkonen, T.M., Graversen, R.G. and Noer, G. (2020) A well-observed polar low analysed with a regional and a global weather-prediction model. *Quarterly Journal of the Royal Meteorological Society*, 146(729), 1740–1767. <https://doi.org/10.1002/qj.3764>.
- Thompson, G. and Eidhammer, T. (2014) A study of aerosol impacts on clouds and precipitation development in a large winter cyclone. *Journal of the Atmospheric Sciences*, 71, 3636–3658. <https://doi.org/10.1175/JAS-D-13-0305.1>.
- Tourville, N., Stephens, G., DeMaria, M. and Vane, D. (2014) Remote sensing of tropical cyclones: observations from CloudSat and A-Train profilers. *Bulletin of the American Meteorological Society*, 96, 609–622. <https://doi.org/10.1175/BAMS-D-13-00282.1>.
- von Storch, H., Langenberg, H. and Feser, F. (2000) A spectral nudging technique for dynamical downscaling purposes. *Monthly Weather Review*, 128, 3664–3673. [https://doi.org/10.1175/1520-0493\(2000\)128<3664:ASNTFD>2.0.CO;2](https://doi.org/10.1175/1520-0493(2000)128<3664:ASNTFD>2.0.CO;2).
- Wootten, A., Bowden, J.H., Boyles, R. and Terando, A. (2016) The sensitivity of WRF downscaled precipitation in Puerto Rico to cumulus parameterization and interior grid nudging. *Journal of Applied Meteorology and Climatology*, 55, 2263–2281. <https://doi.org/10.1175/JAMC-D-16-0121.1>.
- Wu, L.T., Martin, J.E. and Petty, G.W. (2011) Piecewise potential vorticity diagnosis of the development of a polar low over the Sea of Japan. *Tellus A*, 63, 198–211. <https://doi.org/10.1111/j.1600-0870.2011.00511.x>.
- Wu, L.T. and Petty, G.W. (2010) Intercomparison of bulk microphysics schemes in model simulations of polar lows. *Monthly Weather Review*, 138, 2211–2228. <https://doi.org/10.1175/2010MWR3122.1>.
- Yanase, W. and Niino, H. (2007) Dependence of polar low development on baroclinicity and physical processes: an idealized high-resolution numerical experiment. *Journal of the Atmospheric Sciences*, 64, 3044–3067. <https://doi.org/10.1175/JAS4001.1>.
- Yanase, W., Niino, H., Watanabe, S.I., Hodges, K., Zahn, M., Spengler, T. and Gurvich, I.A. (2015) Climatology of polar lows over the Sea of Japan using the JRA-55 reanalysis. *Journal of Climate*, 29, 419–437. <https://doi.org/10.1175/JCLI-D-15-0291.1>.
- Zabolotskikh, E., Bobylev, L., Mitnik, L. and Mitnik, M. (2010) Polar low study using satellite passive and active microwave remote sensing. In: *2010 11<sup>th</sup> Specialist Meeting on Microwave Radiometry and Remote Sensing of the Environment*, IEEE 167–170. <https://doi.org/10.1109/MICRORAD.2010.5559569>.
- Zahn, M. and von Storch, H. (2008a) Tracking polar lows in CLM. *Meteorologische Zeitschrift*, 17, 445–453. <https://doi.org/10.1127/0941-2948/2008/0317>.
- Zahn, M. and von Storch, H. (2008b) A long-term climatology of North Atlantic polar lows. *Geophysical Research Letters*, 35(22). <https://doi.org/10.1029/2008GL035769>.
- Zahn, M. and von Storch, H. (2010) Decreased frequency of North Atlantic polar lows associated with future climate warming. *Nature*, 467(7313), 309–312. <https://doi.org/10.1038/nature09388>.
- Zappa, G., Shaffrey, L. and Hodges, K. (2014) Can polar lows be objectively identified and tracked in the ECMWF operational analysis and the ERA-Interim reanalysis? *Monthly Weather Review*, 142, 2596–2608. <https://doi.org/10.1175/MWR-D-14-00064.1>.

**How to cite this article:** Xue, J., Bromwich, D.H., Xiao, Z. & Bai, L. (2021) Impacts of initial conditions and model configuration on simulations of polar lows near Svalbard using Polar WRF with 3DVAR. *Quarterly Journal of the Royal Meteorological Society*, 147(740), 3806–3834. Available from: <https://doi.org/10.1002/qj.4158>

## APPENDIX A. SUPPLEMENTARY FIGURES

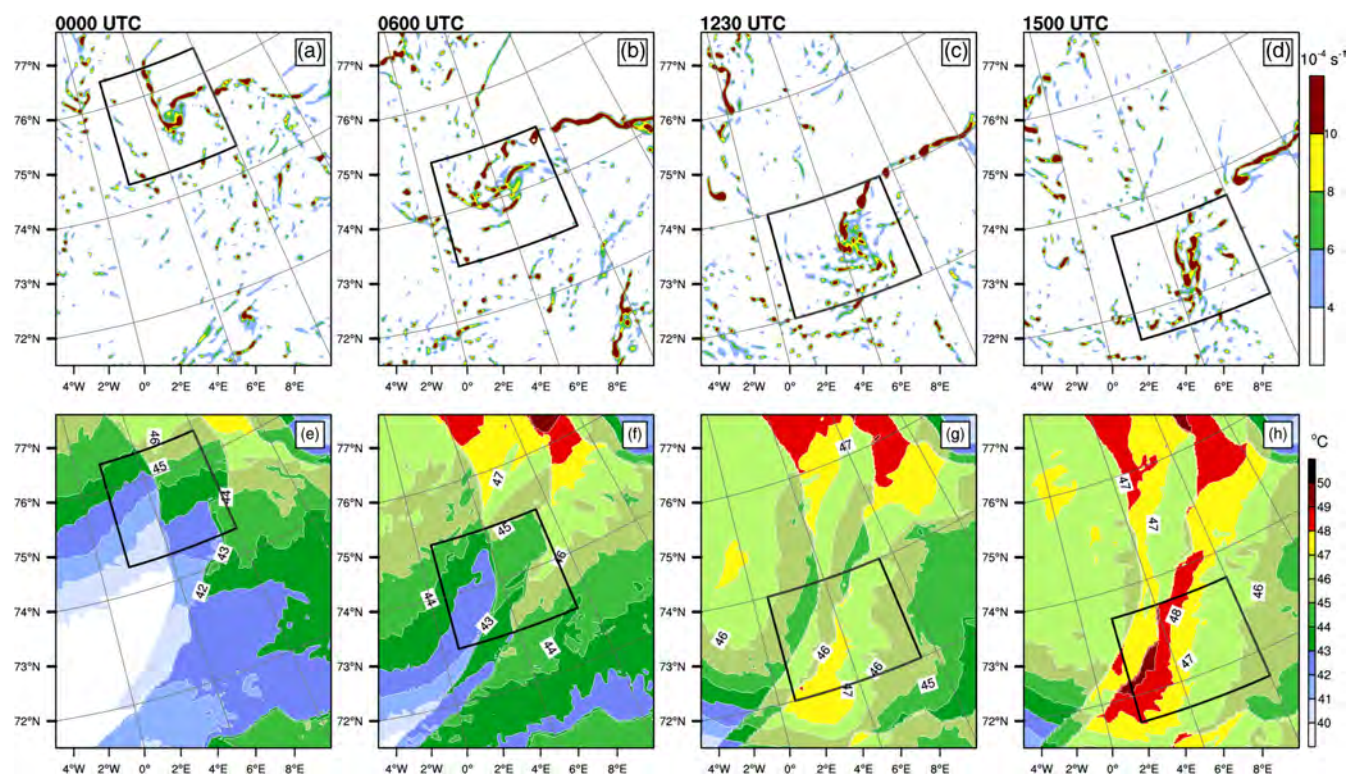


**FIGURE A1** The development of S17 case-study from CR experiment at 0000, 0600, 1230 and 1500 UTC on 26 March (the black box encloses the polar low). (a–d) Relative vorticity at 950 hPa. (e–h) Difference of SST minus T at 500 hPa (SST–T500, °C) [Colour figure can be viewed at [wileyonlinelibrary.com](http://wileyonlinelibrary.com)]

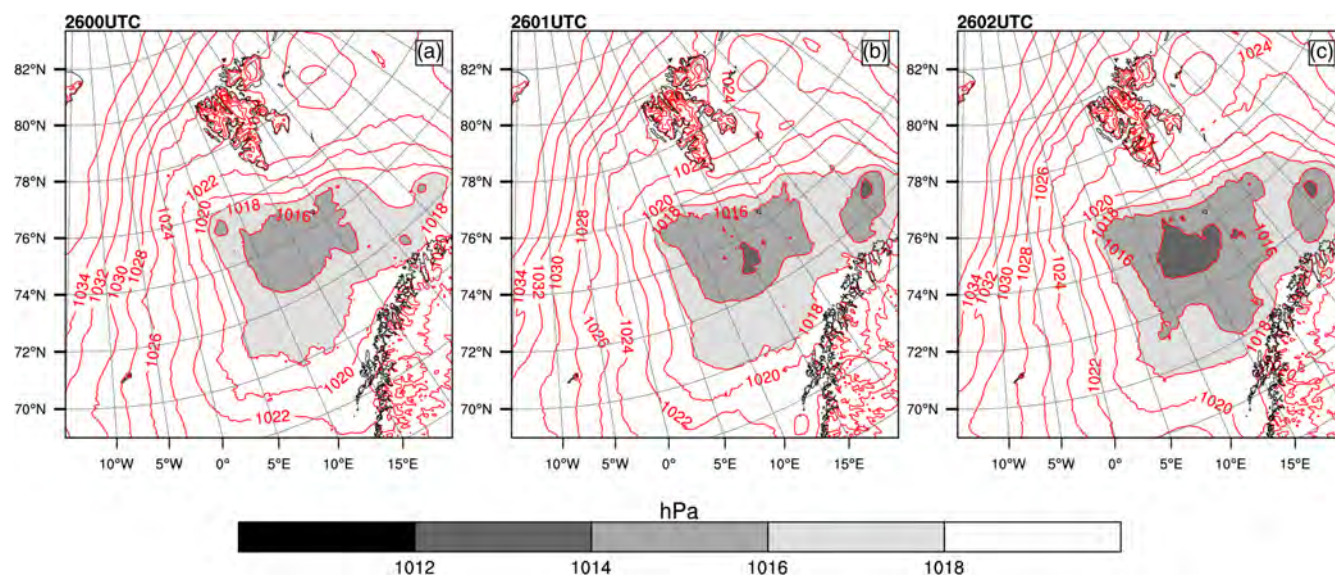


**FIGURE A2** S17 case-study MSLP (red contours, hPa) at (a) 0000 UTC, (b) 0100 UTC and (c) 0200 UTC on 26 March. The grey fills are used to highlight MSLP  $\leq 1,018$  hPa [Colour figure can be viewed at [wileyonlinelibrary.com](http://wileyonlinelibrary.com)]



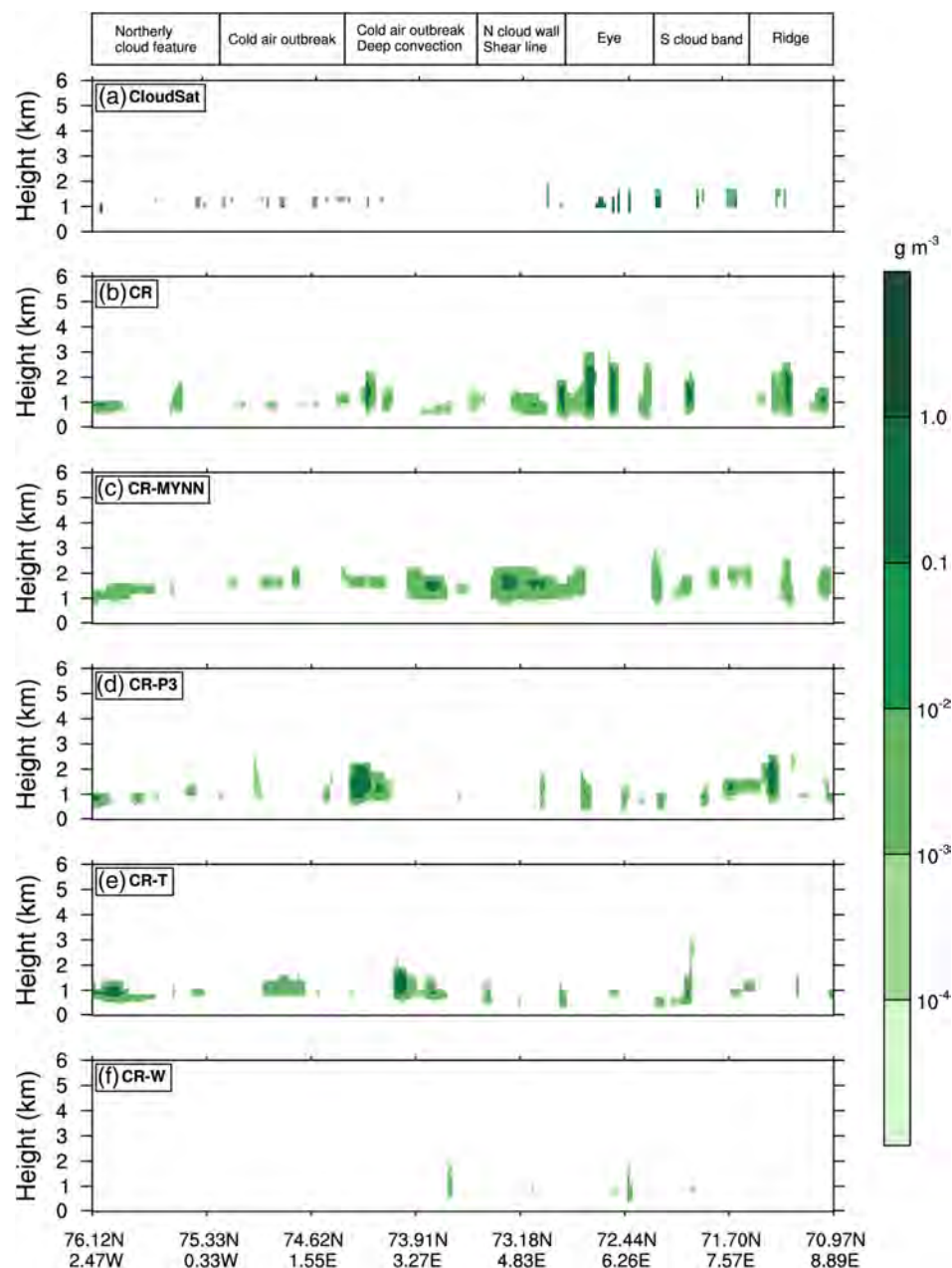


**FIGURE A3** Cloud liquid water content (LWC,  $\text{g m}^{-3}$ ) across the polar low core region for the case-study estimated from CloudSat (following S17) and model outputs at 1130 UTC 26 March. (a) CloudSat, (b) CR, (c) CR-MYNN, (d) CR-P3, (e) CR-T and (f) CR-W. The CloudSat swath that passed from southeast to northwest during 1132–1134 UTC is shown in Figure 1. Feature labels at top are taken from S17 [Colour figure can be viewed at [wileyonlinelibrary.com](http://wileyonlinelibrary.com)]